Journal of Materials Research and Technology 44 (2026) 2181–2198

Contents lists available at ScienceDirect

Journal of Materials Research and Technology

journal homepage: www.elsevier.com/locate/jmrt

Modelling transformation kinetics in spatially graded martensitic–bainitic microstructures of quenched and tempered steel AISI 4140

Benjamin Dollhofer *, Philipp Schüßler, Stefan Dietrich, Volker Schulze

Institute for Applied Materials - Materials Science and Engineering (IAM-WK), Karlsruhe Institute of Technology (KIT), Karlsruhe, 76131, Germany

ARTICLE INFO

Keywords:
Inductive surface hardening
Austempering
Martensitic–bainitic microstructure
Bainite transformation kinetics
AISI 4140 steel

ABSTRACT

Inductive short-time austempering allows the creation of homogeneously distributed and spatially graded martensitic–bainitic microstructures by using a precise temperature control during sample cooling. This study first applies Van Bohemen's bainitic transformation kinetics created for various different steel alloys, to homogenously distributed martensitic–bainitic microstructures in AISI 4140 steel on the laboratory scale. Furthermore, it is transferred to both homogenously distributed and spatially graded martensitic–bainitic microstructures at the component scale. However, the kinetics of bainite transformation exhibit a pronounced dependence on the parent austenite grain size. Consequently, its accurate representation was essential to accurately simulate the surface hardening process. Consistent with established models and their theoretical foundations, the model can be applied to both homogeneous and spatially graded microstructures produced by inductive short-time austempering. This demonstrated its suitability for use at the component scale and provides a solid foundation for the design and optimisation of industrial heat treatment processes.

1. Introduction

Inductive surface hardening has been widely implemented in mechanical, tool, and automotive engineering due to its high energy efficiency and short processing times [1]. Through appropriate process control, inductive surface hardening can also be applied for short-time austempering of components, allowing the transformation of martensitic–bainitic microstructures [2].

For homogeneously distributed microstructures, the presence of a specific volume fraction of bainite has been established to have a beneficial influence on the fatigue strength of the components [3]. A proposed mechanism for this effect is an improved capacity for work hardening [4,5]. Furthermore, a high product of strength and elongation (PSE) is frequently correlated with increased resistance to the initiation and propagation of cracks and can be used as an indicator of fatigue performance [3,6]. In addition, the hardness mismatch between the different fractions within a mixed microstructure is of particular significance, as a great difference is generally understood to promote crack initiation within the softer regions [7–9]. Consequently, achieving elevated hardness in the bainitic areas is of critical importance [3].

High bainitic hardness is usually obtained creating lower bainite, which is formed at comparatively low transformation temperatures [3,10]. Its increased hardness is a result of its fine bainitic needle structure, which also leads to a higher fatigue strength. Within the mixed microstructures, there is also a strengthening contribution of bainite associated with the volumetric change induced by martensite formation. The resulting work-hardening imposed on the existing bainite diminishes as the martensite volume fraction is reduced [11–13]. Additionally, martensitic regions act as crack deflectors for cracks propagating through the bainitic subunits, thus improving the stability against crack growth [3]. In summary, the optimal volume-fraction ratio can be rationalised by the beneficial presence of a specific amount of martensite within the bainitic matrix. For similar chemical compositions, this optimal bainitic volume fraction ranges from 21 % up to 49 % [3,14].

Consequently, to maximise the fatigue life of a surface hardened component, the volume fraction ratio of the martensitic–bainitic microstructure within the surface hardened region must be adjusted. However, transferring the beneficial properties to induction hardening is associated with additional difficulties. During induction surface hardening, high temperature gradients arise, causing various areas of the sample to experience different thermal histories. The austenite grain size is strongly affected by the austenitisation temperature, the heating rate, and the holding time [15–17]. As a result, non-uniform temperature fields result in a heterogeneous distribution of parent austenite grain sizes within the hardened zone. The size of the austenite grain is also known to have a significant influence on the kinetics of bainite [18–22]. Therefore, optimising such treatments at the component scale requires predicting the spatially resolved austenite grain size distribution while explicitly accounting for the non-uniform thermal history. This poses a substantially more complex and computationally expensive problem than the modelling of uniform laboratory samples.

Furthermore, with respect to the adjustment of the volume fraction within the hardened surface layer, Winderlich [23] revealed that local

* Corresponding author.
E-mail address: benjamin.dollhofer@kit.edu (B. Dollhofer).

https://doi.org/10.1016/j.jmrt.2026.08.039
Received 1 June 2026; Accepted 6 August 2026
Available online 14 August 2026

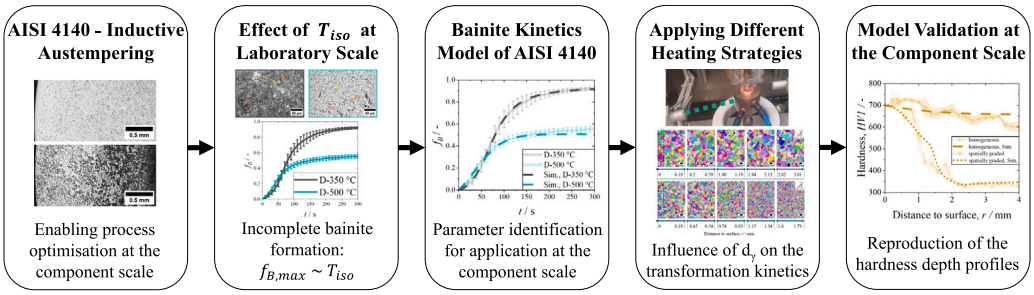

Fig. 1. Methodological framework for advanced process optimisation of inductively austempered parts. To date, no robust predictive model has been available to describe bainite formation during inductive austempering of AISI 4140 under varying heating strategies, and thus to reliably predict and regulate final hardness. By calibrating bainite transformation kinetics models at the laboratory scale, their applicability can be extended to the component scale.

enhancements in fatigue strength can be achieved by minimising spatial gradients in residual stress or hardness profiles. In this regard, the high potential of inductive short-time austempering in reducing the hardness gradient has already been demonstrated [2].

In conclusion, improving the fatigue strength of components manufactured from steels such as AISI 4140 involves two main challenges: achieving a clearly defined balance between lower bainitic and martensitic microstructures, and tailoring the hardness and residual stress distributions so that they match the imposed loading conditions. To use the process at the component scale, where complex temperature histories may arise, an efficient predictive model is required that can capture both homogeneous and spatially graded martensitic–bainitic microstructures.

The goal of this study, as presented in Fig. 1, is to evaluate bainite transformation during inductive austempering to create a model for process optimisation at the component scale. Therefore, the bainite transformation kinetics model proposed by Van Bohemen [24] was adapted to homogenously distributed and spatially graded martensitic–bainitic microstructures in AISI 4140 created by inductive austempering. The model was chosen because it uses relatively few parameters, has been validated for a wide range of steels, and is computationally efficient. In addition, it can be easily integrated into FE simulations, making it well suited for investigations at the component scale.

At first, samples were isothermally austempered at different temperatures T_{iso} to define a model at the laboratory scale. Following Van Bohemen [24], the kinetics of bainite was described using three parameters: the autocatalytic factor λ, and two fitting parameters used to calculate the nucleation rate κ as a function of $w_{\mathrm{c,B}}$ and d_γ. These were calibrated using dilatometry, while the d_γ model combined previous data with current results to predict its evolution for high heating rates. All other model variables were derived from the alloy composition. Secondly, experiments at the component scale were then performed on an induction hardening machine. To favour a lower bainite microstructure, which offers a higher fatigue strength, the austempering temperature T_{iso} was set at approximately 380 °C. Two series were run at the component scale level: one to obtain a homogeneous microstructure and another to generate a graded martensitic–bainitic structure. In both, the isothermal holding time t_{iso} is varied (10 s, 20 s, 45 s) and compared to samples that were directly quenched to room temperature after the heating step.

2. Material and methods

2.1. Material

The material used is the low alloy steel AISI 4140 in a quenched and tempered state. Due to its advantageous balance of strength, toughness and resistance to fatigue, this steel is widely utilised for power transmission components subjected to high mechanical loading [25,26]. The chemical composition of the dilatometry samples (D, laboratory scale) was measured with ICP-OES for Mn, Cr, Si, Mo, and Fe and a CS-Analyser for C. The chemical composition of the samples for inductive short-time austempering (IH, component scale) was measured using a ES 750-CA emission spectrometer from OBLF. Both are presented in Table 1. For both types of samples, the initial microstructure exhibited a hardness of (340 ± 10) HV1 as described in Section 2.4.3.

In Table 2 an overview of all sample groups with the applied procedures is summarised. The process for the dilatometer samples (D) at the laboratory scale was described in Section 2.2.1, the corresponding heat treatments were described in Section 2.3.1. The process for the induction hardened samples (IH) at the component scale was described in Section 2.2.2, the corresponding heat treatments were described in Section 2.3.2.

2.2. Experimental methods

2.2.1. Dilatometer experiments

Dilatometry with the sample group (D) was used to create homogeneously distributed microstructures on a laboratory scale. The dilatometer used for this investigation was a quenching dilatometer DIL 805 by TA Instruments. The samples selected for this study were thin hollow cylinders with an outer diameter of 4 mm, a length of 10 mm and a wall thickness of 0.5 mm. The heating of the samples was controlled by an induction coil and a Type S thermocouple welded to the centre of the sample. The vacuum chamber was evacuated at a pressure of 1×10^{-4} mbar and filled with helium to avoid decarbonisation effects. The change in length of the samples was monitored using a linear variable differential transformer.

2.2.2. Induction hardening experiments

Induction hardening with the sample group (IH) was used to create homogeneously distributed and spatially graded martensitic–bainitic microstructures on a component scale. The experiments were carried out with the FIAND KHM 750 hardening machine, equipped with an IDEA SMS850 dual frequency converter. In Fig. 2 the setup is described. The geometry of the sample used has a diameter of 10 mm within the hardening zone (a). Temperature control of the component was achieved through induction heating and an integrated gas nozzle field in the inductor (b). Temperature monitoring was performed with a pyrometer focused on the hardening zone (c). The pyrometer used was a KTRD 4075-1 model from Dr. Georg Maurer GmbH, which had a measuring range of 300 °C to 1500 °C. The pyrometer measurements demonstrated reproducibility with a reproducibility of ±5 K. After isothermal holding, the samples were quenched to room temperature using a quenching shower with a water-polymer cooling agent (d).

Table 1
Chemical composition of the samples in percentage mass fraction w%.

		Fe	C	Mn	Cr	Si	Ni	Mo
(D)	mean	bal.	0.434	0.795	1.105	0.256	0.05	0.197
	sd	–	0.01	0.02	0.05	0.03	0.03	0.01
(IH)	mean	bal.	0.459	0.757	1.102	0.183	0.17	0.185
	sd	–	0.013	0.003	0.006	0.003	0.001	0.002

Table 2
Overview of the sample groups and the applied procedures.

Sample group name	Description	Microstructure
D-RT	dilatometer sample, quenched after austenitisation	homogeneously distributed
D-T_{iso}	dilatometer sample, isothermally austempered at temperature T_{iso} (see Table 3)	homogeneously distributed
IH-RT-H	induction hardened sample, quenched after austenitisation	homogeneously distributed
IH-t_{iso}-H	induction hardened sample, isothermally austempered at qty380°C for t_{iso}.	homogeneously distributed
IH-RT-G	ind. surface hardened sample, quenched after austenitisation	spatially graded
IH-t_{iso}-G	ind. surface hardened sample, isothermally austempered at qty380°C for t_{iso}.	spatially graded

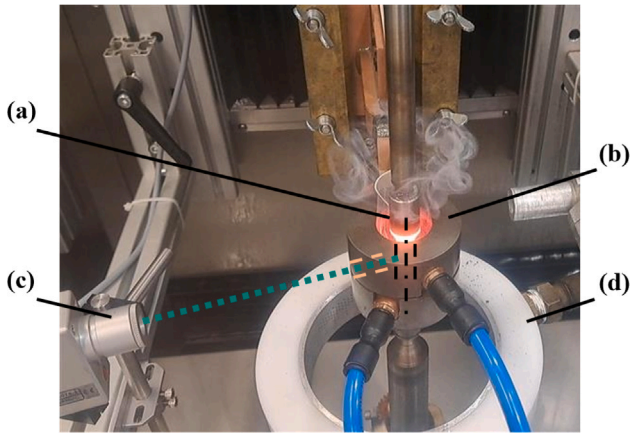

Fig. 2. (a) sample, (b) inductor featuring an opening for pyrometer measurement and fittings for air supply, (c) pyrometer (d) quenching shower [27].

2.3. Heat treatment procedures

2.3.1. Laboratory scale: Dilatometry

Initially, experiments were conducted at the laboratory scale to investigate bainite transformation kinetics under precisely controlled thermal conditions. In Fig. 3 the schematic development of the temperature (red line) and strain (grey dashed line) during dilatometer experiments is shown. In a first step, each sample was heated for a duration of 60 s to a temperature of 920 °C. This step was followed by a holding step, maintaining this temperature for 60 s to fully austenitise the samples. Subsequently, the samples were quenched in 2 s to the dedicated T_{iso}. To ensure that the mixed microstructure created is only consistent of martensite or bainite, the isothermal holding time t_{iso} was determined from the finish line of the bainitic region of the AISI 4140 TTT diagram [28]. An exception is the heat treatment conducted at 475 °C, where t_{iso} is selected such that the strain rate change remains below 10^{-4} %s^{-1}. In this case, no substantial variation in $f_{B,max}$ is expected with increasing t_{iso} In Fig. 3, this finish line of the isothermal bainite transformation is schematically represented as a green line at the end of the austempering steps. In Table 3, an overview of T_{iso} is given with the corresponding t_{iso}. The strain curve shown in Fig. 3, which was exemplary for a T_{iso} of 350 °C, is a measure of the progress of the bainite transformation, which is explained in more detail in Section 2.5. In addition, directly quenched samples were analysed following the same austenitisation process without austempering to create a fully martensitic sample as a reference (D-RT, blue line).

The method proposed by Van Bohemen and Hanlon [29] focuses on assessing the strain after quenching following austempering in the bainitic temperature range. By comparing this strain of the D-T_{iso} samples and the strain of the D-RT samples, it was possible to determine the martensitic volume fraction $f_{\alpha'}$. A schematic illustration of the determination of $f_{\alpha'}$ is shown in Fig. 4. The calculation of the martensitic volume fraction from the experimental data is shown in Eq. (1):

$$f_{\alpha'} = \frac{\Delta\varepsilon_{T,i}}{\Delta\varepsilon_{\alpha'}} \tag{1}$$

The strain measured after direct quenching was used to obtain the corresponding $\Delta\varepsilon_{\alpha'}$. Therefore, the austenite region was theoretically extended by drawing the dashed line using its thermal expansion coefficient as its slope (see Fig. 4). The difference between these two values at the same temperature is set as $\Delta\varepsilon_{\alpha'}$. Subsequently, the values of $\Delta\varepsilon_{T,i}$ were determined after austempering at different T_{iso} and subsequent quenching to room temperature. Additionally, it was necessary to determine the volume fraction of retained austenite after quenching f_{γ}. The volume fraction of bainite f_B can then be determined with Eq. (2):

$$f_B = 1 - f_{\alpha'} - f_{\gamma} \tag{2}$$

The maximum attainable bainitic volume fraction $f_{B,max}$ at a given isothermal temperature was used to infer the time-dependent evolution of the bainite fraction from the measured strain progression.

2.3.2. Component scale: Inductive short-time austempering

The inductive short-time austempering heat treatment comprises two different process routes. Fig. 5 shows a schematic development of the temperature at the surface for both processes. To illustrate how an alternative austenitisation route affects the subsequent transformation behaviour, identical austempering times t_{iso} were used for both sample sets, namely 10 s, 20 s, and 45 s. As discussed in the introduction, the optimal bainite volume fraction is considered to lie between

Table 3
Overview of austempering temperatures and corresponding austempering times of the (D) samples.

T_{iso} :	350 °C	375 °C	400 °C	425 °C	450 °C	475 °C	490 °C	500 °C	510 °C	525 °C
t_{iso} :	312 s	300 s	325 s	600 s	2000 s	5200 s	2000 s	1500 s	1300 s	1170 s

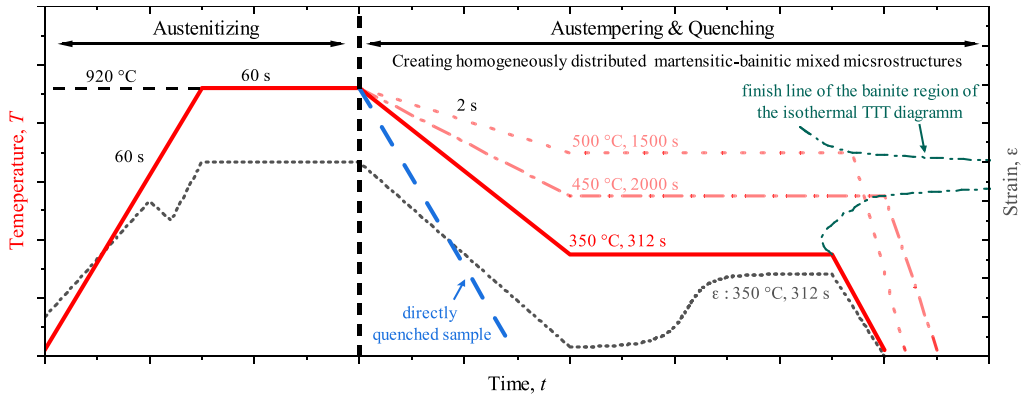

Fig. 3. Schematic illustration of the dilatometer experiment; Development of the temperature T and the strain ε as dashed line.

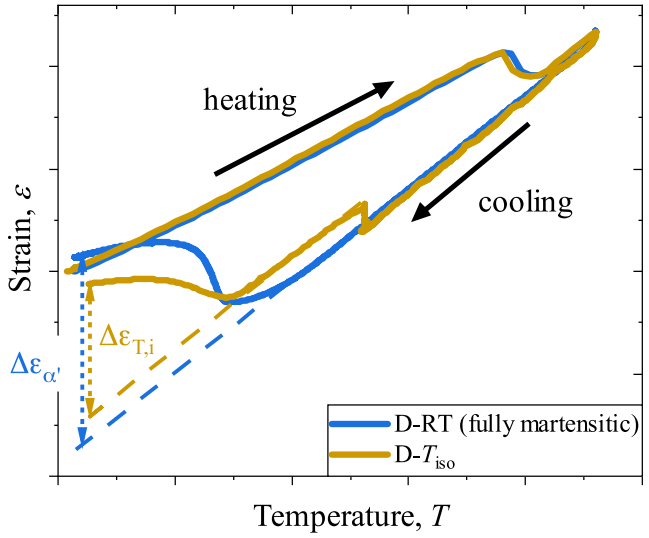

Fig. 4. Schema of the determination of $f_{\alpha'}$ according to Van Bohemen and Hanlon [29].

21 % and 49 % [3,14]. Previous investigations have shown that, using a similar austenitisation approach, such volume fractions can be attained within the holding time range considered in this study [27]. For comparison, an additional set of samples in each group was quenched directly after austenitisation.

In the first series of experiments, the samples were fully austenitised before austempering (IH-t_{iso}-H), similar to the dilatometer experiment (Fig. 5(b)). This sample group first experienced heating in 3 s with an inductor frequency of 13 kHz and a generator power of 68 kW. The relatively low frequency was chosen to have a homogeneous heating of the part. The highest recorded surface temperature reached approximately 1100 °C. The heating step was followed by an air quenching to an isothermal holding temperature of 380 °C that took approximately 20 s.

During the second series of experiments, the samples (IH-t_{iso}-G) were austenitised only in the surface area to create a spatially graded microstructure (Fig. 5(a)). This sample group first experienced rapid heating to the same measured temperature on the surface of around 1100 °C in 400 ms with an inductor frequency of 175 kHz and a generator power of 153 kW. This was followed by an air quenching to a stable temperature of 380 °C that took approximately 14 s.

Afterwards, the austempering step was similar for both series of experiments. The selected holding temperature of 380 °C ensured that the sample remained above the martensite start temperature M_S, which was calculated to be approximately 315 °C [30]. The temperature was controlled for the corresponding t_{iso}, with an inductor frequency of about 15 kHz and a generator power between 4 kW to 32 kW. A lower frequency was chosen to create a more homogeneous temperature distribution within the sample during austempering. Following the austempering step, the samples were quenched to room temperature using a quenching shower. The cooling agent for this quenching step was a mixture of water and polymer. The average cooling rate was roughly 1600 K s^{-1} as determined by measurements with a pyrometer and a thermocouple.

2.4. Metallographic characterisation

2.4.1. X-ray diffraction

To estimate the value of the retained austenite within the dilatometer samples after quenching, X-ray diffraction (XRD) was performed using a D2 phaser (Bruker Corporation, USA). The diffraction patterns were recorded in Bragg–Brentano geometry with θ/θ focusing. Using a Cu-Kα X-ray tube characterised by a wavelength of $\lambda_{CuK\alpha}$ = 1.5406 Å and operated at 30 kV and 10 mA, measurements were performed in the angular range of 10° to 145° (2θ). The 2θ step size was maintained at 0.01°, with each step having an acquisition duration of 384 s. To improve statistical reliability, the sample was rotated. To determine the retained austenite fraction, the four-point method according to the ASTME975 standard was used [31]. Using the integrated intensity of the diffraction peaks of ferrite (bcc, (200) and (211) planes) and austenite (fcc, (200) and (220) planes) diffraction peaks, the retained austenite content was calculated by the peak area ratios between the two phases. If no distinct austenite peaks were observed, it can be inferred that the austenite fraction was below 1 %.

2.4.2. EBSD measurement

Electron backscatter diffraction (EBSD) analysis was utilised for reference measurement of the austenite grain size of the sample group (IH). Therefore, a Helios NanoLab 650 SEM (FEI, Thermo Fisher Scientific Inc., USA) with an e-Flash HD detector (Bruker Corporation, USA) was used. Scans were conducted using an acceleration voltage of 20 kV and a beam current of 6.4 nA on a pre-tilted surface of 70°. The total map resolution was set to 638 × 424 pixels with a step size of 51 nm

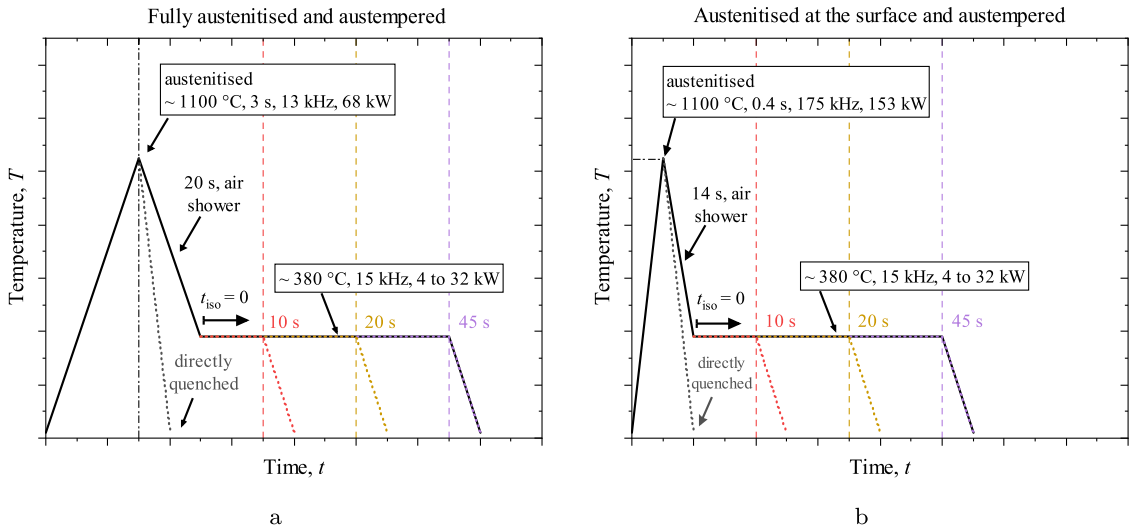

Fig. 5. Schematic illustration of the surface temperature history of the induction hardening experimental heat treatment; (a) heated for 3 s with medium frequency (MF, 13 kHz) to fully austenitise the sample; (b) heated for 0.4 s with high frequency (HF, 175 kHz) to surface harden the sample.

with a 7 ms/px exposure time for the electronic backscatter pattern. The study uses the MTEX 5.10.2 toolbox in MATLAB for analysis [32]. The parent grain boundaries were obtained with the method described by Niessen et al. [33].

2.4.3. Hardness measurement

The hardness measurement was performed with a Qness Q10A micro-hardness tester using the Vickers method with a test weight of 1 kg (HV1) or 0.1 kg (HV0.1) according to DIN EN ISO 6507-1 [34]. To obtain additional insight into the microstructure, each sample in group (D) underwent four hardness measurements using HV0.1. As suggested and analysed in earlier studies [20,27], the hardness of the martensitic–bainitic microstructure can be used to estimate the bainitic volume fraction. Because uniform strain monitoring was not achievable at the component scale to determine f_B, the hardness of the sample group (IH) was used for the evaluation. Consequently, the hardness depth profiles of the samples were determined in HV1, using three measurement points for each distance from the surface.

2.4.4. Optical analysis

The samples were initially ground and polished to a surface finish of less than 1 µm. They were then etched for 3 s in 2 % Nital and examined by light microscopy. In martensitic–bainitic microstructures, the pronounced dark-etching areas can be associated with inter- and intracementite precipitates located within the lower bainite sheaves [35].

2.5. Modelling the transformation of bainite

During the past century, many models have been proposed to describe the bainite transformation, with an ongoing debate as to whether it is mainly diffusion-controlled or diffusionless [36–38]. There are also different modelling strategies, notably phase-field simulations of bainitic transformations, which provide sophisticated tools to visualise microstructural evolution and intricate morphologies [39]. However, their broader adoption is frequently constrained by substantial computational demands, the need for extensive parameter calibration, and reliance on modelling assumptions that are not invariably subjected to rigorous validation [20].

In this work, the physically based model proposed by Van Bohemen [24] was chosen and adjusted for application to AISI 4140. The model captures the kinetics of bainite formation by explicitly accounting for both nucleation behaviour and displacive growth, and it has been validated for multiple steel grades. Most of its parameters can be obtained from empirical relations based on the chemical composition of the steel (see Table 5), which ensures low computational cost. Moreover, the analytical formulation enabled its direct incorporation into FE simulations, thus supporting robust evaluations at the component scale.

Essentially, the model is a modified Johnson–Mehl–Avrami–Kolmogorov equation, which has been refined progressively over the years [40,41]. Eq. (3) shows the calculation of the transformation rate of the bainitic volume fraction f_B, the nucleation factor κ and the autocatalytic factor λ.

$$\frac{df_B}{dt} = (1 - f_B)(1 + \lambda f_B)\kappa \tag{3}$$

The difference in this model from previous studies [40] was that κ was not used directly as a fitting parameter. Instead, it was calculated with respect to the mechanical stabilisation of austenite during the transformation of bainite. In Eq. (4), κ is already shown in simplified form:

$$\kappa = \nu^* \frac{6 N_S V_n}{d_\gamma} \frac{\Gamma_B (B_{S^*} - T)}{(G_{e,0} + \Delta G_{e,B})} \exp\left(-\frac{K_1 \Gamma}{R}\right) \exp\left(-\frac{Q_b}{RT}\right) \tag{4}$$

The equations needed to calculate κ were listed in Table 5 in the Appendix [24,29,30,40,42]. Regarding chemical compositions, the percentage by mass of alloying element i was marked as w_i. In this study, the carbon content within the remaining austenite $w_{c,\gamma}$ was used and set as a function of the progressive transformation of bainite. As described in Eq. (5), $w_{C,\gamma}$ was calculated using the lever rule:

$$w_{C,\gamma} = \frac{w_{c,total} - f_B \cdot w_{c,B}}{1 - f_B} \tag{5}$$

The carbon content in bainite $w_{C,B}$ is used as a temperature-dependent fit parameter, as applied in previous studies [24,43]. Therefore, $w_{C,B}$ reflects both, the resolved carbon content in the bainitic ferrite and the carbides within the bainitic subunits. In conclusion, three fit parameters remain to calculate bainite transformation, namely λ, $w_{C,B}$, and d_γ.

Finally, an important measure for the interpretation of bainite kinetics was provided by the definition of T_{nose}, which was established as the isothermal temperature that exhibits the maximum κ at the beginning of the transformation. This temperature is commonly identified as the nose on the TTT diagram and was specified in Eq. (6) [41]:

$$T_{nose} = -\frac{Q_b}{2R} + \frac{1}{2} + \sqrt{\left(\frac{Q_b}{R}\right)^2 + 4\frac{Q_b}{R} B_S} \tag{6}$$

For the given chemical composition, T_{Nose} equals (475 ± 9) °C for both sample groups. In addition, the incubation time for the bainite transformation was derived from the bainite start curve of the TTT diagram [28].

2.6. Modelling the parent austenite grain size

It is well established in the literature that the parent austenite grain size d_γ has a strong impact on the formation of bainite [20]. It influences whether bainite nucleates at grain boundaries or within grains [19], and the transformation rate is strongly grain size dependent [18]. However, the effect of the parent austenite grain size is not straightforward. It has been shown that when the growth of bainitic sheaves is faster than their nucleation at the parent austenite grain boundaries, coarser parent austenite grains increases the rate of bainite formation. In contrast, when boundary nucleation is faster than sheaf growth, refinement of the parent austenite grain size accelerates the transformation kinetics.[21,22].

In the context of spatially graded microstructures, modelling of d_γ was essential to describe the kinetics of bainite transformation. During the induction surface hardening process, significant temperature gradients occur. As a result, there are large differences in the maximum temperature and the holding time during austenite transformation across the corresponding section. Therefore, d_γ should change with the distance from the surface r to the area of the initial microstructure. To predict d_γ during the process, a model introduced by Wang et al. [16] was modified and fitted to higher temperatures and heating rates.

$$d_\gamma = ({d_{\gamma,0}}^m + A \cdot t^n)^{1/m} \tag{7}$$

The parameter $d_{\gamma,0}$ represents the initial grain size of austenite. The parameters m, n and A describe the growth of the austenite grain. Similarly to the literature, n was set constant to 0.823 and the parameter A was calculated with an Arrhenius approach:

$$A = 1.154 \times 10^{13} \cdot \exp\left(-\frac{Q_A}{RT}\right), \tag{8}$$

with $Q_A = 236\,317.26\,\mathrm{J mol^{-1}}$, R as the ideal gas constant and T as the transformation temperature. A quadratic fit function was introduced to calculate m:

$$m = -9.053 + 0.0191 \cdot T - 7.03 \times 10^{-6} \cdot T^2. \tag{9}$$

These parameters were modified based on an earlier study that employed higher heating rates compared to those used in the literature [16]. The data base for the model is provided in Table 6 in the Appendix.

2.7. Simulation framework

The simulations are carried out in Abaqus Standard 2024, augmented with user-defined subroutines. Python was used to manage the control mechanisms and data exchange across the electromagnetic and thermal-mechanical simulations including the models explained in the previous sections. The structure of the simulation and the material model used were based on previous work by Schwenk [44] and Kaiser [45,46]. In addition, the simulation model has been described and developed in previous publications [47–49].

To predict the austenitisation process, the transformation kinetics employed for the simulation were modelled using a modified JMAK equation with established parameters [50,51]. The Koistinen–Marburger model determines the volume fraction of martensite with α_M and M_S also set to depend on $w_{C,\gamma}$ (see Table 5):

$$f_{\alpha'} = 1 - \exp(-\alpha_{M,w_{C,\gamma}}(M_{S,w_{C,\gamma}} - T)) \tag{10}$$

The hardness was evaluated using the empirical Hollomon–Jaffe method [52]. Therefore, its incremental description for non-isothermal heating [53] adapted to AISI 4140 [54] was used to calculate the dimensionless parameter $H_{P,i}$:

$$H_{P,i} = H_{P,i} - 1 + \frac{T_i}{2.303 \cdot 10^{\frac{H_{P,i-1}}{T_i - C}}} \cdot \Delta t \tag{11}$$

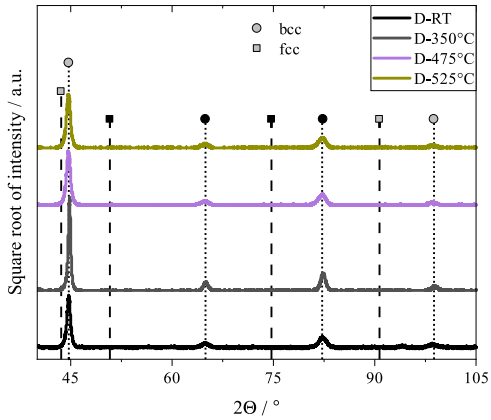

Fig. 6. XRD results of the (D) samples (D-RT, D-350 °C, D-475 °C, D-525 °C). The calculated peak positions of bcc and fcc were marked with circles or squares. The positions filled in black were used for the calculation of the retained austenite fraction.

The coefficient C was calculated to 18.78 [52]. $H_{P,i}$ was numerically integrated over time and calculated for each volume fraction separately. Consequently, the hardness of the different volume fractions HV_x was determined by their transformation temperatures without interaction between the volume fractions:

$$HV_x = 1079.8 - 0.0396 \cdot H_{Px} \tag{12}$$

3. Results

3.1. Dilatometer experiments

To determine f_B with Eq. (2), the volume fraction of retained austenite f_γ was first determined. Fig. 6 shows the intensity of the XRD as a function of the 2θ angle. For the entire batch, no austenite peaks were detected that could be evaluated according to the standard. As a result, Eq. (2) could be reduced to:

$$f_B = 1 - \frac{\Delta\varepsilon_{T,i}}{\Delta\varepsilon_{\alpha'}} \tag{13}$$

Fig. 7(a) shows the development of the maximum possible bainite fraction $f_{B,max}$ and the corresponding $f_{\alpha'}$ for different isothermal temperatures using Eq. (13). The maximum bainitic volume fraction, $f_{B,max}$, remained nearly constant, decreasing only slightly from an average of 94 % to 86 % up to T_{nose}. Beyond this temperature, it dropped markedly, reaching just 7 % at 525 °C. In addition, the average hardness for the isothermal temperature was plotted, showing the increase in hardness with increasing $f_{\alpha'}$.

Fig. 8(a) shows a micrograph of a D-350 °C sample with a remaining amount of $f_{\alpha'}$ as bright areas and f_B as dark etching areas. For the upper bainit temperature range, Fig. 8(b) shows a micrograph of D-525 °C with a high amount of $f_{\alpha'}$ and a small amount of f_B.

Fig. 9 shows the transformation of bainite for individual isothermal austempering temperatures T_{iso} from 350 °C to 525 °C. Fig. 9(a) shows that the maximum transformation rate df_B/dt initially increased from 1 %s^{-1} to 1.9 %s^{-1} as T_{iso} was increased within the temperature interval from 350 °C to 425 °C. Within this temperature range, the value of $f_{B,max}$ was approximately (93 ± 2) %. Fig. 9(b) indicates that df_B/dt remains essentially constant at about 1.9 %s^{-1} up to T_{nose} = 475 °C, while $f_{B,max}$ decreases from 93 % to 87 %. Fig. 9(c) shows that when T_{iso} exceeds T_{nose}, both df_B/dt and $f_{B,max}$ drop markedly, reaching on average only 0.05 %s^{-1} and 7 %, respectively. In addition, the results were plotted on the TTT diagram in Fig. 9(d), illustrating their evolution within the bainitic region. They showed that the temperature associated with the maximum transformation rate changes significantly from 475 °C to about 425 °C once the bainitic volume fraction f_B exceeded 70 %.

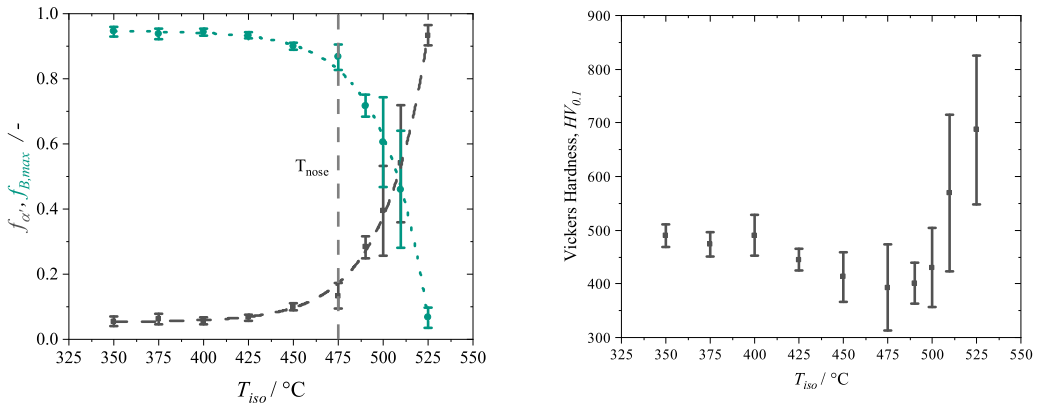

Fig. 7. Development of f_B, $f_{\alpha'}$ (a) and $HV_{0,1}$ (b) for different isothermal temperatures after holding until the end of the bainite region.

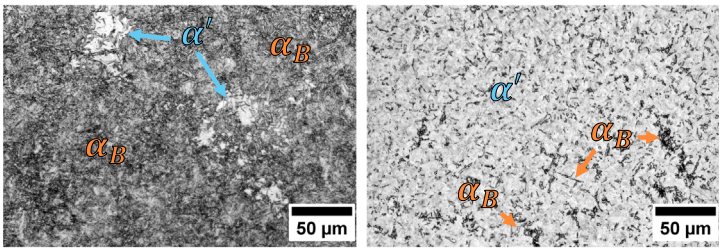

Fig. 8. Light microscopy of D-350 °C (a) and D-525 °C (b) samples after polishing and etching for 3 s with 2% Nital; ferritic martensite α' as bright and ferritic bainite α_B as dark areas.

3.2. Hardness measurements of induction hardened samples

In Fig. 10 an overview of the fully austenitised sample group and the surface hardened group can be seen with their corresponding micrographs. The different colours consistently indicate the distinct isothermal holding times t_{iso} (10 s, 20 s, 45 s) as well as the samples that were quenched directly.

Fig. 10(a) displays the hardness measurements of fully austenitised sample groups. For all samples, a modest decrease in hardness could be detected from the surface towards the centre of the part, ranging from about 770 HV1 to 680 HV1 for the IH-RT-H sample and from roughly 700 HV1 to 580 HV1 for the IH-45 s-H sample. The IH-RT-H and IH-10 s-H did not show significant differences in their hardness depth curves. A noticeable decrease in the depth profile of the hardness was observed only for 20 s and 45 s isothermal holding times. Fig. 10(b) presents micrographs, with the IH-RT-H sample above and the IH-t_{iso}-H samples below. For an isothermal holding time t_{iso} of 20 s, and even more distinctly for 45 s, dark etching clusters of bainitic volume fraction are visible across the cross-section.

Fig. 10(c) illustrates the hardness depth profiles of surface-hardened samples. Even for low t_{iso}, a significant decrease in hardness compared to IH-RT-G could be observed. Near the surface, this effect was less pronounced, with hardness values decreasing only from 754 HV1 to 652 HV1, determined by comparing the mean values of IH-RT-G and IH-45 s-G. However, when examining the same samples at a hardening depth of 1 mm, the hardness decreased more markedly, from 780 HV1 to 432 HV1. Fig. 10(d) shows the micrographs of the IH-RT-G sample above and the IH-t_{iso}-G samples below. These are illustrating an increase in the bainitic volume fraction from the transition zone of the initial microstructure to the surface, having pronounced dark clusters of bainite.

3.3. Simulation results

3.3.1. Model at the laboratory scale

In order to show the effect of carbon dependence, these results were also compared with van Bohemen's models without carbon dependence [24,40]. Fig. 11 shows the best-fitting models obtained both with and without allowing $w_{C,\gamma}$ to evolve, together with the corresponding experimental data from the dilatometer experiment. The resulting fit parameter for $w_{C,B}$ and λ could be expressed as functions of T_{iso}, given in K, with $T_{nose} = 748$ K.

$$w_{c,B} = \begin{cases} 0.385\ , T_{iso} <= T_{nose} \\ 5.31 - T_{iso} \cdot 6.64 \times 10^{-3}\ , T_{iso} > T_{nose} \end{cases} \quad (14)$$

$$\lambda = \begin{cases} 4.76 \times 10^{12} \cdot \exp(-T_{iso} \cdot 0.043) + 22.56\ , T_{iso} <= T_{nose} \\ 179.55 - T_{iso} \cdot 0.225\ , T_{iso} > T_{nose} \end{cases} \quad (15)$$

These equations are valid only in the observed range below 525 °C. When T_{iso} exceeds this temperature, they were set to 0. With the given temperature history for austenitisation at the laboratory scale, d_γ was calculated to 13.5 µm as described in Section 2.6. The calculated and determined maximum volume fractions of bainite $f_{B,max}$ are listed in Table 4:

The model that incorporates the temporal evolution of $w_{C,\gamma}$ reproduces the experimental data with root mean square error (RMSE) values ranging from 0.6 % to 6 %. A notable outlier is the case shown in Fig. 11(f), which deviates substantially from the model and results in an RMSE of 18 %. For temperatures below 500 °C, the average RMSE is 2.6 %. However, the model that does not account for the evolution of $w_{C,\gamma}$ achieves robust predictions for $f_B < 0.7 \cdot f_{B,max}$, with a mean RMSE of 2.8 %, again apart from the experiment conducted at a holding temperature of 525 °C, which exhibits an RMSE of 13 %.

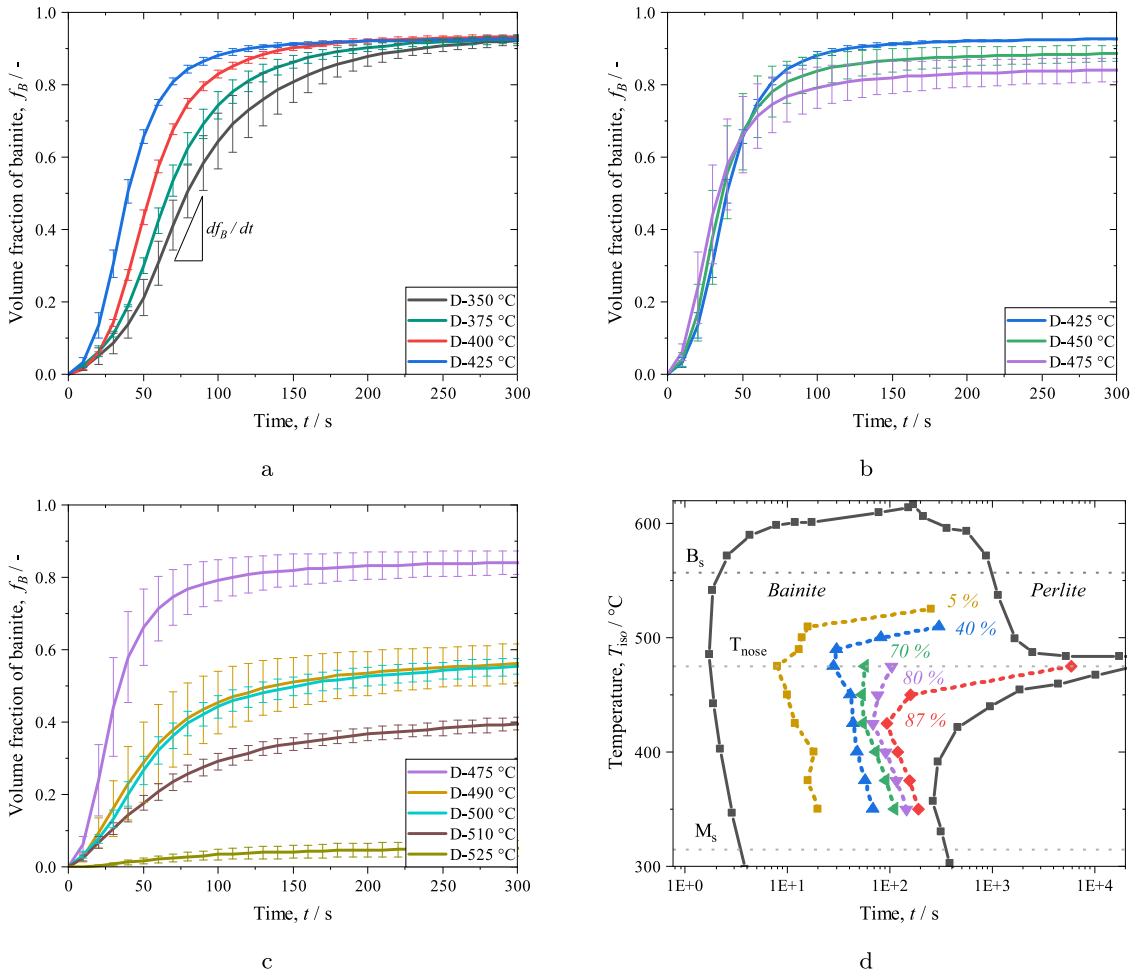

Fig. 9. Transformation of bainite for different isothermal austempering temperatures from 350 °C to 525 °C (a, b, c) as well as its transfer to the TTT-diagram [28] of the bainite region (d).

Table 4
Determined and calculated $f_{B,max}$ for the investigated isothermal austempering temperatures.

T_{iso} :	350 °C	375 °C	425 °C	475 °C	500 °C	525 °C
$f_{B,max}$ exp.:	(94 ± 2) %	(93 ± 2) %	(93 ± 1) %	(87 ± 1) %	(61 ± 14) %	(7 ± 3) %
With $w_{C,\gamma}$ evol.:	95 %	94 %	91 %	86 %	51 %	26 %
No $w_{C,\gamma}$ evol.:	100 %	100 %	100 %	100 %	99 %	93 %

3.3.2. Induction hardening heat treatment

As described in Section 2.3.2, induction surface hardening at the component scale differs from the experiments at the laboratory scale, as they include regions subjected to heterogeneous and temporally non-uniform thermal histories during heating or quenching. This implies that d_γ is expected to exhibit a heterogeneous distribution along the cross section of the sample. To further validate the model developed for the determination of d_γ, EBSD measurements were conducted at various distances from the sample surface after the austempering step. The EBSD analysis performed on the IH-20 s-H and IH-20 s-G samples is presented in Fig. 12. Based on the images, the mean values for d_γ and its standard deviation were quantified using the line-intersection method. The IH-20 s-H sample shows no variation in the radial direction, with an average d_γ of 9.5 µm, suggesting only minor differences in heating and cooling conditions across its cross section. In contrast, the IH-20 s-G sample, examined in the surface-hardened region, displays a pronounced decrease in d_γ from an average of 7.6 µm at the surface to 3.5 µm at a depth of 1.6 mm.

Fig. 13 depicts both the simulated evolution, using Eq. (7), and the experimentally determined profile of d_γ as a function of r. For both sample sets, the d_γ distributions are presented for the directly quenched condition as well as for the states produced by the applied austempering strategies.

The modelled d_γ generally matched the average values of the EBSD measurements. However, because d_γ exhibits a large standard deviation, the model did not capture local variations.

During inductive heating at the component scale, the resulting temperature distributions caused the effective bainite transformation times t_B to differ from the isothermal holding time t_{iso} specified for process control. Fig. 14(a) shows the simulated results at the component scale for t_B as a function of r. For example, setting t_{iso} to 10 s resulted in a t_B of approximately 20 s for both samples groups. Similar deviations could be seen for the other samples. In regions that were fully austenitised, t_B remained nearly unchanged across the entire depth range in both sets of samples. Only the sample IH-45 s-G showed minor deviations within the transition zone leading to the initial microstructure. Conditions involving direct quenching to room temperature are not shown, since no bainite was formed in the IH-RT-H or IH-RT-G sample groups in the simulation.

The variation of the bainitic volume fraction with distance from the surface is presented in Fig. 14(b). For different heating strategies but

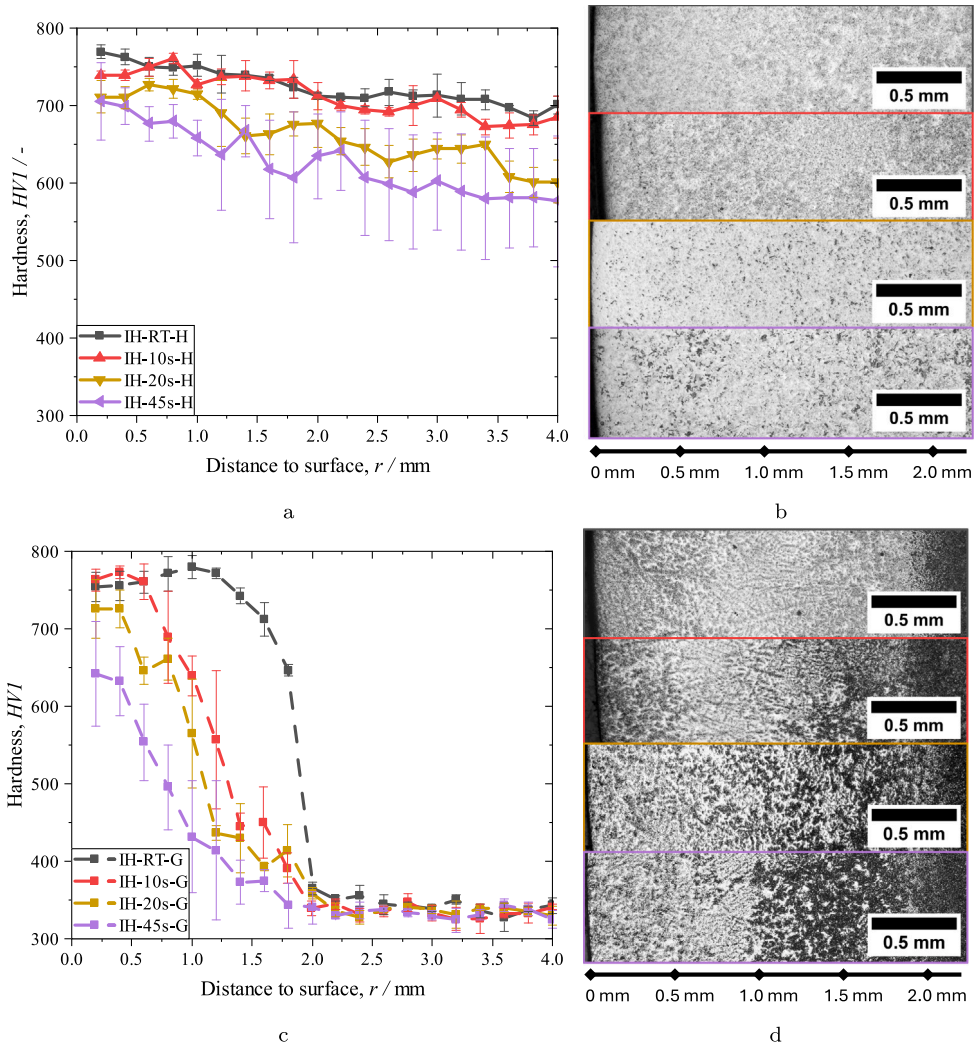

Fig. 10. Comparison of the hardness depth profile for IH-RT-H and IH-t_{iso}-H samples (a) with the corresponding micrographs (b). Comparison of the hardness depth profile for IH-RT-G and IH-t_{iso}-G samples [27] (c) with the corresponding micrographs (d). For the micrographs the samples were polished to < 1 μm and etched with 2 % Nital for 3 s.

identical isothermal holding times, the values of f_B are nearly identical in the near-surface region and only begin to diverge significantly at larger depths.

Fig. 15 displays the simulated and experimentally determined hardness profiles for the homogeneously heated samples IH-t_{iso}-H and the surface hardened samples IH-t_{iso}-G. For all samples, a reduction in hardness with increasing bainitic volume fraction was observed. For the spatially graded samples, small amounts of the original microstructure were still present at distances greater than 1.8 mm from the surface, which led to an additional decrease in hardness in both the model and the experimental results. On average, the RMSE between the simulated hardness profiles and the experimental measurements is 42 HV1 for the homogeneously distributed and 40 HV1 for the spatially graded microstructure.

4. Discussion

4.1. The incomplete reaction of bainite

The results of the dilatometer experiment showed the necessity of accounting for the incomplete transformation of bainite, especially at isothermal holding temperatures T_{iso} exceeding 475 °C, which is equal to T_{nose}. The reduction in $f_{B,max}$ observed in Fig. 7(a) with increasing T_{iso} is consistent with the behaviour reported previously in the literature [24,55]. This is confirmed by the dilatometry-based hardness data in Fig. 7(b), where the higher martensite fractions $f_{\alpha'}$ at elevated T_{iso} align with an increased hardness. Consistent differences in the bainitic volume fraction f_B can also be observed in the micrographs etched with 2 % Nital shown in Fig. 8, where the samples with T_{iso} of 350 °C exhibit a significantly higher f_B than those treated at 525 °C. Thus, understanding the order of magnitude of the incomplete reactions at different T_{iso} is important to capture the transformation behaviour when complex temperature fields, such as in induction hardening, occur.

The modelling approach for the incomplete reaction assumes primarily a mechanical stabilisation of austenite during the bainite transformation. This stabilisation increases the elastic strain energy G_e, which in turn leads to a reduction in the nucleation rate κ. The mechanisms governing the incomplete transformation of bainite, in terms of progressive stabilisation of austenite during transformation, are described in detail by Van Bohemen [24]. In his study, the bainite transformation is divided into three distinct stages. In the initial stage of bainite transformation, dislocation strengthening is considered to be the primary mechanism responsible for the stabilisation of the remaining austenite and therefore for determining the transformation rate [56,57]. In a second stage, the growth of bainite sheaves from different nucleation sites at the austenitic grain boundary leads to mutual impingement. Consequently, the role of geometric constraints

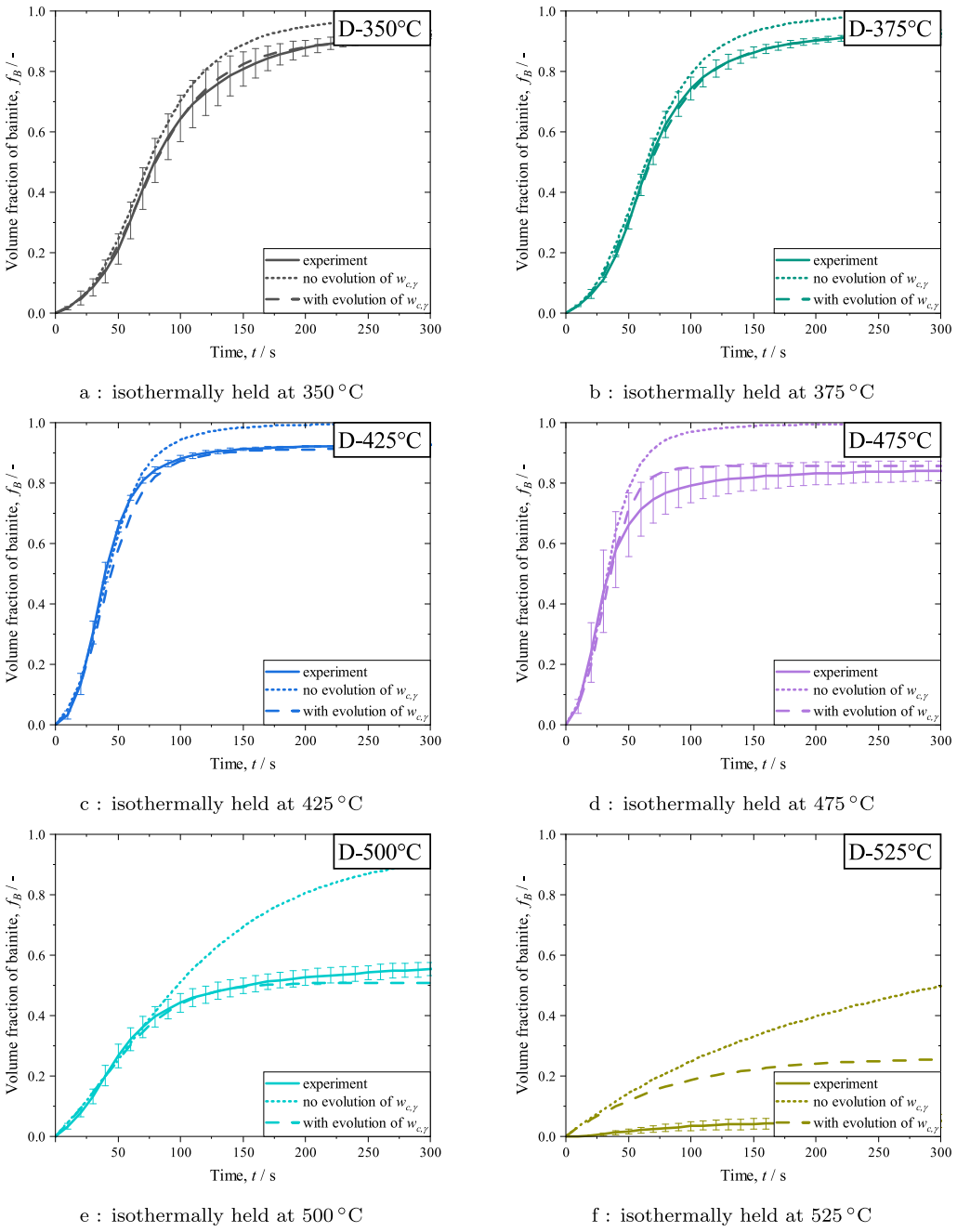

Fig. 11. Comparison of the model created by Van Bohemen [24] with one model that accounts for the evolution of $w_{C,\gamma}$ during the progression of bainite transformation and one model without evolution of $w_{C,\gamma}$.

becomes increasingly significant [58–60]. In the final stage of the transformation, it is hypothesised that the hydrostatic pressure within the residual austenite increases, thus contributing to its stabilisation [61]. The latter situation occurs once the volume fraction of bainite exceeds the critical percolation threshold, p_c, which is associated with the breakdown of the austenite percolation network [10,62].

The nucleation rate κ is of central importance for the transformation (see Eq. (4)):

$$\kappa = \nu^* \frac{6 N_S V_n}{d_\gamma} \frac{\Gamma_B (B_{S^*} - T)}{(G_{e,0} + \Delta G_{e,B})} \exp\left(-\frac{K_1 \Gamma}{R}\right) \exp\left(-\frac{Q_b}{RT}\right)$$

As T_{iso} increases, the magnitude of G_e decreases. Numerically, at the end of the transformation, this results in a G_e of 987 Jmol^{-1} for T_{iso} at 350 °C, 748 Jmol^{-1} for T_{iso} at 425 °C and 600 Jmol^{-1} for T_{iso} at 475 °C, obtained using $G_e = G_{e,0} + \Delta G_{e,B}$ [24]. Although the activation energy $Q^* = K_1 \Gamma \times T + Q_b$ [24] increases linearly with temperature, the exponential factor of the model increases as T_{iso} increases. Accordingly, in the lower range of transformation temperatures, both terms increase the nucleation rate κ as T_{iso} increases. As a reference, the maximum transformation rate increases from 1 %s^{-1} in 350 °C to 2 %s^{-1} in 425 °C, as shown in Fig. 9(a). Within this temperature range, the maximum bainitic volume fraction $f_{B,max}$ shows only a marginal reduction, decreasing from 94 % to 93 %. As T_{iso} approaches 475 °C, the transformation rate is found to stagnate and $f_{B,max}$ decreases from 93 % to 87 %, as shown in Fig. 9(b). At a transformation temperature of 525 °C, the maximum transformation rate decreases significantly to 0.05 %s^{-1}, and the maximum attainable bainite fraction, $f_{B,max}$, is limited to 7 %, as shown in Fig. 9(c). Transferring this finding to the TTT diagram, as illustrated in Fig. 9(d), shows that only minor volume

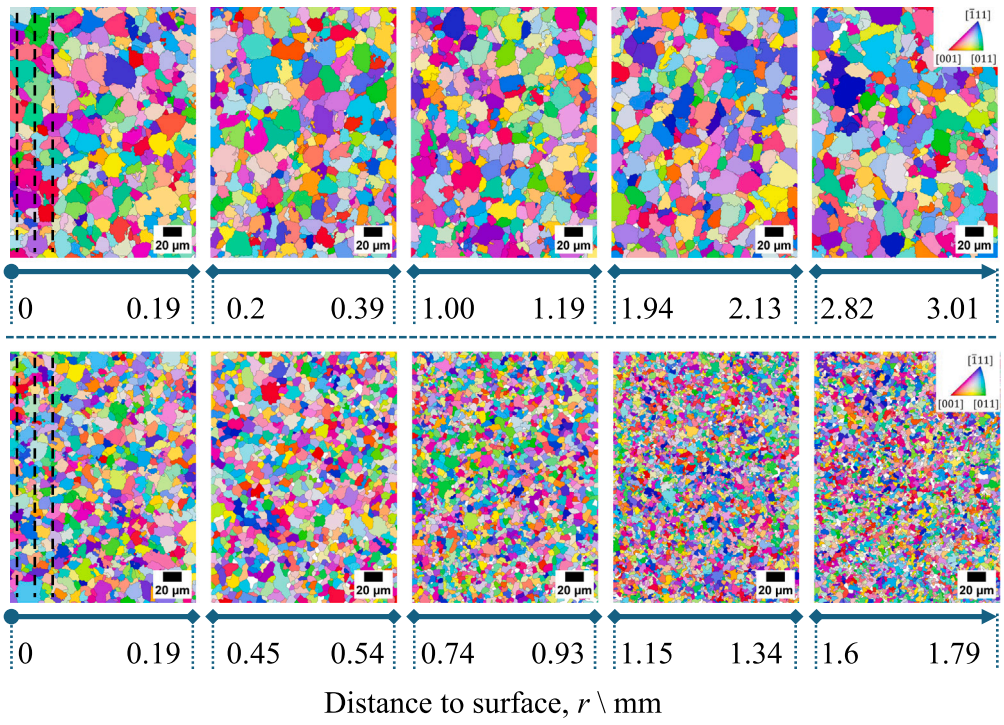

Fig. 12. Parent austenite reconstruction with MTEX 5.10.2 toolbox in MATLAB and the method described by Niessen et al. [33]; IH-20s-H profile above and IH-20s-G below.

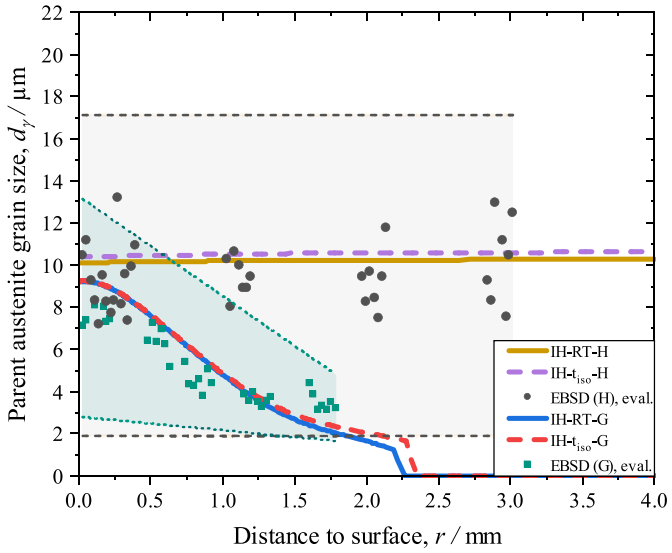

Fig. 13. Comparison between the measured and simulated austenite grain size d_γ of the IH-RT and the IH-t_{iso} samples.

fractions of bainite form at temperatures above T_{nose} of 475 °C. Furthermore, the figure shows that, as the bainitic transformation progresses, the temperature associated with the maximum transformation rate progressively changes from 475 °C to 425 °C.

This behaviour results from the steadily decreasing net driving force, $G_{net} = \Gamma_B(B_{S^*} - T)$, as the transformation temperature increases. Consequently, the model explains the incomplete reaction at temperature T primarily by this decrease in G_{net}. Thus, the decisive factor is the decrease in the starting temperature of the bainite for stabilised austenite, given by $B_{S^*} = B_S - (\Delta B_{S,\sigma_\gamma} + \Delta B_{S,B})$. During an isothermal transformation, B_{S^*} gradually converges towards the corresponding T_{iso}. Accordingly, at the instant this condition is met, κ becomes zero and the transformation stops. Starting from the initial calculated B_S value of 556 °C [30], B_{S^*} theoretically reaches T_{iso} after about 1901 s for a transformation at 350 °C. This exceeds the investigated holding time of 312 s determined by the TTT-diagram [28], but only leads to a small deviation in $f_{B,max}$ from 93 % in the experiment to 95 % as maximum in the current model. Furthermore, for a transformation at 475 °C, T_{iso} was reached after about 116 s and after about 196 s for a transformation at 500 °C.

The temperature-dependent contribution to austenite stabilisation, $\Delta B_{S,\sigma_\gamma}$, increases only from 25 % to 50 % of the stabilising influence provided by pre-existing bainite, $\Delta B_{S,B}$. Consequently, the formation of bainite remains the primary factor governing the stabilisation of austenite. In the model, changes in $\Delta B_{S,B}$ become less pronounced if the evolution of the carbon content in the remaining austenite, $w_{C,\gamma}$, is neglected. In this case, B_{S^*} is predicted to reach T_{iso} after about 2107 s at 350 °C, around 600 s at 475 °C, about 1392 s at 500 °C, and exhibits substantial variations in $f_{B,max}$ at the end of the transformation (see Fig. 11). As described in Table 4, the discrepancies in $f_{B,max}$ become particularly significant at elevated transformation temperatures. At 350 °C, the experiment yielded a mean value of (94 ± 2) %, while the model that accounts for changes in $w_{C,\gamma}$ predicts 93 %, and the model that ignores such changes predicts 100 %. Instead, at a transformation temperature of 500 °C, the experiment resulted in a mean value of (61 ± 14) %, while the model that accounts for changes in $w_{C,\gamma}$ predicts 51 %, and the model that neglects such changes predicts 93 %.

However, as illustrated in Fig. 11, both approaches reproduce the experimental behaviour well below 70 % of the experimental $f_{B,max}$, even for temperatures above T_{nose}. This can also be observed in the literature [24]. In situations where the bainite volume fraction is small, the error introduced by neglecting carbon redistribution remains correspondingly limited. For higher values of f_B, it is necessary to account for the retardation effect caused by carbon redistribution [29,43]. Furthermore, it raises the question of why the incomplete reaction is sensitive to $w_{C,\gamma}$ and why this effect is particularly pronounced at high transformation temperatures of bainite.

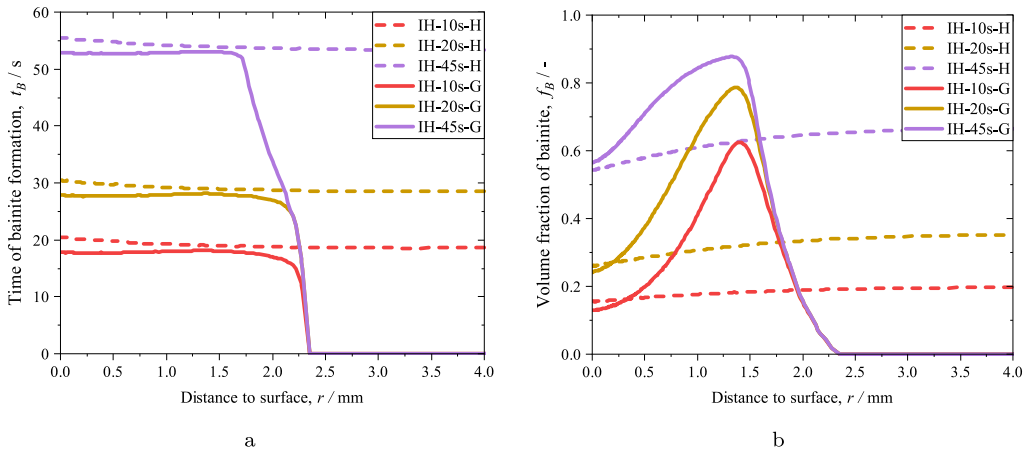

Fig. 14. Total time of bainite transformation of the IH-t_{iso}-G sample group as a function of the distance to the surface (a) and its corresponding bainitic volume fraction (b).

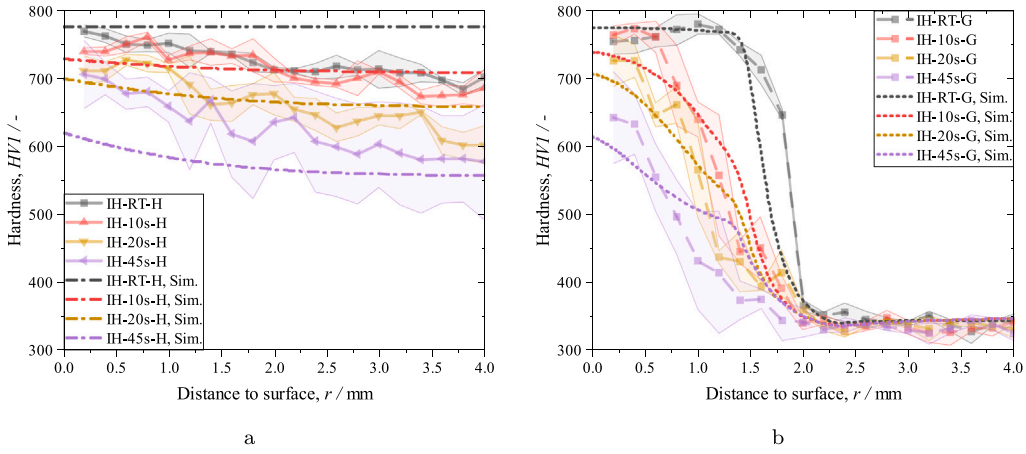

Fig. 15. Comparison between simulated and measured hardness profiles of the IH-t_{iso}-H samples (a) and the IH-t_{iso}-G samples (b).

4.2. Influence of the carbon redistribution

A bainite sheaf is a cluster of several platelets, also known as subunits, all of which have the same orientation and size [20]. Timokhina et al. [63] observed that during the formation of the sheaves, $w_{C,\gamma}$ initially increases in adjacent austenite regions. Although local variations are mainly ascribed to the autocatalytic factor λ, the general increase in $w_{C,\gamma}$ has a strong impact on κ as previously described in Section 4.1.

The importance of $w_{C,\gamma}$ evolution during bainitic transformation in the determination of $f_{B,max}$ has previously been highlighted in the literature [29,43]. In these studies, the key parameter is the carbon concentration in a given volume fraction of bainite $w_{C,B}$, which is assumed to remain constant during transformation and to depend solely on the austempering temperature T_{iso}. For the current model, because a direct measurement of $w_{C,B}$ is challenging when only a small fraction of retained austenite is present in the microstructure, its evolution is determined by fitting, as outlined in Eq. (14). Furthermore, $w_{C,B}$ is assumed to be constant at a value of 0.385 wt% for all T_{iso} up to 475 °C. For higher temperatures, it drops markedly, with, for example, 0.18 wt% at 500 °C.

Bhadeshia and Edmonds [64] demonstrated the incomplete reaction's sensitivity to T_{iso}, and stated a highly reduced transformation rate in the upper bainite region. This was attributed to the different transformation mechanisms between upper and lower bainite. Upper bainite is typically described as an aggregate of bainitic ferrite that forms without carbide precipitation, whereas lower bainite is characterised by the presence of these carbide precipitates [20]. It was also noted that, in the isothermal transformation, either lower or upper bainite was formed but never a mixture. Since $w_{C,B}$ accounts for both the dissolved carbon in bainitic ferrite and the carbides present within the bainitic subunits, it can be assumed that $w_{C,B}$ is markedly lower when the transformation occurs in the upper bainite regime since there are no carbide precipitates within the sheaves. With respect to the lever rule, a larger amount of carbon is redistributed in the remaining austenite per volume fraction of bainite when $w_{C,B}$ decreases. Furthermore, during the bainite formation process, this increase in carbon enrichment in the remaining austenite explains the reduction in κ in the upper bainite region, leading to the pronounced decrease in the transformation rate above T_{nose}.

Fig. 16 presents the corresponding carbon content of the remaining austenite $w_{C,\gamma}$, at the end of bainitic transformation for various T_{iso}, and compares it with the findings of Van Bohemen and Hanlon [29] and Ravi et al. [43], who examined steels with a comparable but lower overall carbon content in their microstructure. In all cases $w_{C,\gamma}$ decreases with increasing transformation temperature. The model accounts for this behaviour by predicting a small decrease in the maximum attainable fraction of the bainite volume, $f_{B,max}$, even at lower transformation temperatures. However, small deviations appear in the temperature range above T_{nose}. As mentioned above, according to the lever rule in Eq. (5), a decrease in $w_{C,B}$ leads to a faster increase in $w_{C,\gamma}$ as the bainitic transformation proceeds. Consequently, in the current model, at temperatures just above T_{nose}, the final carbon content of the remaining austenite, $w_{C,\gamma}$, increases again slightly. Since the maximum attainable bainite volume fraction $f_{B,max}$ decreases significantly at

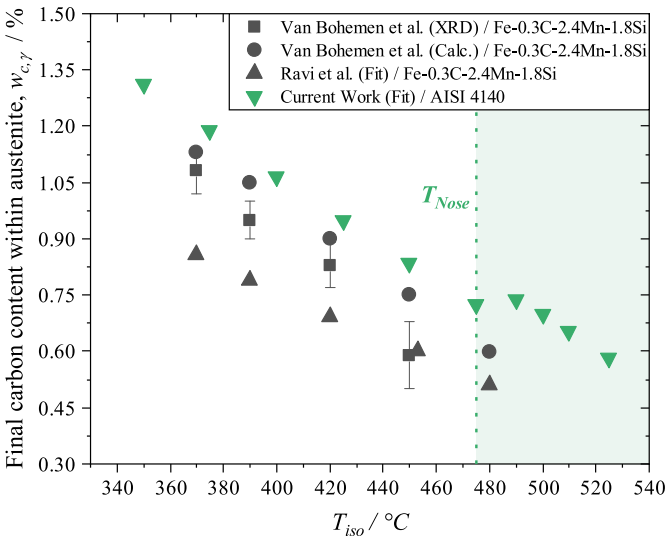

Fig. 16. Development of the final $w_{C,\gamma}$ for different T_{iso}.

higher temperatures (see Fig. 7(a)), $w_{C,\gamma}$ then decreases and converges to $w_{C,total}$ as $f_{B,max}$ approaches zero. The consistency between the model predictions, the current experimental results and previously published studies supports the reliability of the selected value of $w_{C,B}$ for the present study.

As discussed in Section 4.2, the overall driving force G_{net} continues to decline, although $w_{C,\gamma}$ decreases with increasing temperatures. The pronounced decrease in bainite formation observed for temperatures above 475 °C can be attributed to the increased carbon redistribution associated with the formation of upper bainite [63]. Nevertheless, the current model has demonstrated limitations at temperatures exceeding 500 °C.

4.3. Influence of the morphology of bainite

According to Chang and Bhadeshia [65], the aspect ratio of the bainitic sheaves increases as its formation temperature increases T_{iso}, defining the aspect ratio as the ratio between the thickness of the sheaf and its length. Consequently, an increase in T_{iso} could result in a reduction in the critical percolation threshold p_c, if it is assumed that the volume of the bainite sheaves remains constant [62]. As a result, at higher isothermal temperatures T_{iso}, the remaining austenite becomes insulated earlier, and the final stage of the bainite transformation, stabilisation of austenite due to increased hydrostatic pressure, can be achieved for lower f_B. However, accurately determining and comparing p_c between different T_{iso} values is challenging, not least because the volume of the bainite sheave is likely to change as T_{iso} changes.

At the level of the bainite subunits or laths, Van Bohemen [42] proposed a method to determine their thickness, within a sheaf, for various T_{iso} values. To calculate the lath thickness L_B, the yield strength of austenite at a certain temperature $\sigma_{\gamma,T}$ is compared to its lower limit strength σ_{lim} (see Table 5):

$$L_B = \frac{2}{\sigma_{\gamma,T} - \sigma_{lim}} \tag{16}$$

Using Eq. (16) the magnitude of L_B for a T_{iso} of 350 °C is about 0.15 μm at the beginning and 0.07 μm at the end of the transformation. The reduction in L_B during bainite formation is ascribed to the increase in $w_{C,\gamma}$ and its influence on the yield strength of austenite. As $w_{C,\gamma}$ increases, $\sigma_{\gamma,T}$ grows more rapidly than σ_{lim}, which in turn leads to an increase in L_B [42]. At a transformation temperature of 475 °C, the calculated values are about 1.4 μm at the beginning and decrease to 0.49 μm at the end of the transformation. Consequently, L_B decreases as the bainite transformation progresses and increases with higher austempering

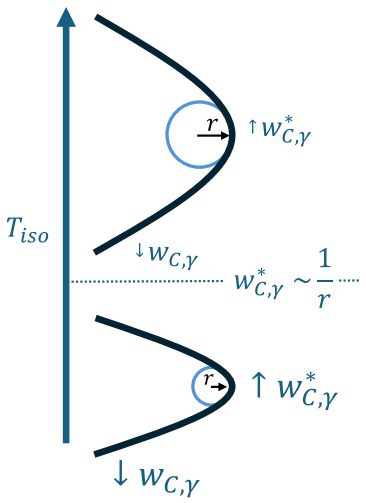

Fig. 17. Influence of the aspect ratio and curvature radius r on autocatalytic factor λ deviated from the conclusions of Bhadeshia and Christian [20]. A decreased r increases the carbon content in the remaining austenite at the tip of the needle $w^*_{C,\gamma}$ while it decreases the carbon content $w_{C,\gamma}$ along the sides. This effect is reduced for higher temperatures and is therefore also reducing λ.

temperatures. This also indicates that geometrical constraints become increasingly significant at higher austempering temperatures, lowering the maximum formation rate of bainite. Furthermore, at a temperature where $\sigma_{\gamma,T}$ is very close to σ_{lim}, it is suggested that granular bainite is formed [42]. This change in morphology may also involve different transformation mechanisms. In this study, the limit is exceeded at temperatures of about 500 °C. Consequently, it is reasonable to conclude that the model presented here is only valid for temperatures below this threshold, as indicated by the pronounced discrepancy between simulation and experiment shown at 525 °C in Fig. 11(f).

4.4. Autocatalytic factor and parent austenite grain size

The autocatalytic factor is closely related to the morphology of the bainite subunit. Derived from the experimental result in Section 3.1, λ showed a constant behaviour for transformation temperatures below T_{nose}. An exception is λ at very low transformation temperatures. This is attributed to an increase in dislocation in the remaining austenite [66] or a reduction in lath thickness L_B in temperatures close to M_S [42]. Consequently, this reduction in L_B results in an increase in the interface boundaries of the bainite laths within the remaining austenite, leading to an increase in λ [66,67].

Furthermore, λ, L_B, and the change in the distribution of $w_{C,\gamma}$ are interrelated. In theory, the elevated dislocation density at the tip of a bainite subunit results in a local increase in $w^*_{C,\gamma}$ [68]. Therefore, $w_{C,\gamma}$ on the lateral faces is decreasing, which stimulates autocatalytic nucleation [66]. The increase in $w^*_{C,\gamma}$ at the tip also depends on its curvature, decreasing this effect with an increase in the curvature radius [20,68]. As illustrated in Fig. 17, an increase in T_{iso} could lead to a larger radius of curvature as the thickness of the lath increases. This may also explain the decrease of λ observed at temperatures above 475 °C, since in the remaining austenite the difference between the carbon content at the tip, $w^*_{C,\gamma}$, and the difference at the lath sides becomes less pronounced.

In a recent investigation, Avila et al. [22] provided a detailed description of how autocatalysis is related to the grain size of austenite. Their analysis supports the experimental findings of Matsuzaki and Bhadeshia [21], which demonstrated that, when bainitic sheaves grow more rapidly than they nucleate at the boundaries of the parent austenite grains, larger austenite grains promote faster bainite formation. In contrast, when nucleation at boundaries outpaces sheaf growth,

reducing the grain size of the austenite enhances the transformation kinetics. With their model, they could predict whether a decrease in d_γ accelerates or retards the transformation of bainite. According to them, λ serves as a general indicator of the balance between grain-boundary nucleation and autocatalytic nucleation. This behaviour is attributed to the difference in the activation energies, $\Delta Q = Q_{GB} - Q_A$. Here, Q_{GB} is the activation energy for nucleation at the grain boundary and Q_A is that for autocatalytic nucleation. For low ΔQ the bainite transformation is accelerated by smaller d_γ. They further demonstrated that increasing $w_{C,\gamma}$ or T_{iso} increases ΔQ, thereby promoting grain-boundary-controlled nucleation [22]. In addition, the predicted evolution of f_B for bainite formation governed by grain-boundary nucleation is consistent with the development shown in Fig. 9(c) for T_{iso} above 475 °C.

As described in Section 4.2, the carbon present in the retained austenite is redistributed during the formation of bainite. Timokhina et al. [63] further reported that, as the transformation time increases, the carbon concentration within the austenite becomes progressively more homogeneous. In addition, this redistribution proceeds more rapidly at higher transformation temperatures [69]. As a result, this behaviour might represent a contradiction. A more homogeneous distribution of $w_{C,\gamma}$ could also decrease the distinction between nucleation at the boundary of the parent austenite grain and autocatalytic nucleation, thereby lowering ΔQ at elevated transformation temperatures. Nevertheless, because Caballero et al. [69] observed this effect after several hours of austempering, it is unclear to what extent this mechanism is applicable to the present study.

In the applied model, the dependence of λ on the austempering temperature accounts for the distinction between nucleation at grain boundaries and autocatalytic nucleation. The close agreement between the prediction of the model, the experimental data, and the theory of autocatalysis substantiates the robustness of the fitted evolution of λ used in the current study.

4.5. Bainite transformation at the component scale

Once λ and $w_{C,B}$ are fitted, it is possible to describe changes in df_B/dt within the model of Van Bohemen [24], only by changing d_γ. In contrast to earlier approaches [24,40], λ does not exhibit an explicit dependence on d_γ. Consequently, it is assumed that the autocatalytic process itself is not affected by grain size, whereas its impact on bainite transformation is. The parameter strongly affected by d_γ is the nucleation rate κ. At the component scale, the model does not require any adjustment of λ when d_γ is modified.

The literature indicates that, if the grain volume distribution is known, the influence of a heterogeneous parent austenite grain size distribution can be determined by superposing the contributions of individual grains without resorting to an average size [70]. This approach is motivated by the presence of a plateau in bainite formation caused by carbon precipitates within the austenite or bainitic ferrite. Since no such explicit plateau was observed in the experiments, only the mean parent austenite grain size was adopted.

Fig. 10 illustrates the high dependence of the hardness on the bainitic volume fraction. The large error bars observed for samples subjected to longer austempering times in Figs. 10(a) and 10(c) are attributed to intrinsic microstructural heterogeneity. As the bainitic volume fraction increases, the microstructure evolves into a more mixed martensitic–bainitic microstructure, so that individual hardness indents can measure locally differing phase fractions, which in turn amplifies the scatter in the data. This interpretation is further supported by the micrographs in Figs. 10(b) and 10(d), where the distribution of the bainitic volume fraction through the section is illustrated. While micrographs are highly sensitive to sample preparation and can be challenging to interpret, grey needle-like features are typically classified as martensite or tempered martensite, while darker regions are attributed to bainite [35]. Although the bainitic volume fraction appears macroscopically uniform across the section or distance to surface, the bainite forms in localised clusters. The variation therefore represents material heterogeneity rather than experimental uncertainty and cannot be markedly decreased.

Consequently, one of the main observations from the depth profiles of the hardness in Fig. 10 is that, although using the same austempering route, the resulting hardness still varies significantly between the different heating strategies. As the samples were austempered at the same temperature of about 380 °C, this difference does not arise from an incomplete reaction, but rather from pronounced variations in transformation kinetics, which are governed by changes in the parent austenite grain size d_γ. In the current case, a reduction in d_γ accelerates the rate of bainite formation. For a comparable overall carbon content, this observation is in agreement with the results reported in the literature [71]. Consequently, for AISI 4140 at an isothermal holding temperature T_{iso} of approximately 380 °C, the activation energy for nucleation at the grain boundary must not be significantly higher than the activation energy for autocatalytic nucleation [21,22].

In Fig. 14(a), it can be seen that the effective bainite transformation time t_B remains nearly constant within the hardened zone, the only deviation occurring in the sample group IH-45 s-G. This is because, in the depth interval from 1.8 mm to 2.2 mm, the material was not fully austenitised. In this area, the hardness has essentially reached that of the initial microstructure at 340 HV1, and f_B is below 20 %. As a result, the maximum attainable f_B had already been achieved for the t_B values shown for the sample group IH-45 s-G. In summary, the variation in f_B has to be predominantly governed by the corresponding variation in d_γ.

Based on the evolution of the parent austenite grain size presented in Fig. 13, it can be concluded that, on the surface of both homogeneous and spatially graded samples, the comparable effective time to form the bainite t_B and the grain size of the austenite d_γ lead to a similar volume fraction of bainite. As a result, these conditions produce nearly identical surface hardness values for both sample types. This can be concluded by the experiment and the simulation as shown in Fig. 15(b).

The profile of d_γ is primarily determined by the heating and austempering conditions, with the exception of the air cooling to T_{iso}. This is also evident in Fig. 13, which compares the austempered and directly quenched samples. Air cooling to T_{iso} had only a minor effect on the evolution of d_γ. The slight increase observed can be attributed to lower cooling rates at greater depths and to the extent of the heated region, both of which result in longer transformation times of the parent austenite.

In conclusion, although the transformation times to bainite are almost identical for the IH-t_{iso}-H and IH-t_{iso}-G sample series, they result in completely different f_B values, as illustrated in Fig. 14. This indicates that, by tailoring the thermal history applied to the sample, it is possible to further adjust the distribution of d_γ over r and, consequently, the hardness profile during austempering.

In Fig. 18, the simulated bainitic volume fraction is additionally compared with the findings of an earlier study that examined a similar sample as in the present work [49]. In this previous study, different methods were investigated to analyse the bainitic volume fraction for a spatially graded martensitic–bainitic mixed microstructure. It can be observed that, compared to the experimental results, f_B is slightly overestimated in the present transformation kinetics model. However, in the transition zone to the original microstructure, the experimental method could not reliably differentiate between bainite and tempered martensite, which explains the deviations observed at depths greater than 1.5 mm from the surface. Additionally, the hardness prediction in the model does not account for any contribution from bainite hardening caused by martensitic transformation [11–13], which may lead to an underestimation of the hardness predicted in the model.

The model yields RMSE values of 42 HV1 for homogeneously distributed microstructures and 40 HV1 for spatially graded microstructures, with corresponding average standard deviations of about 25 HV1 and 19 HV1, respectively. Although the RMSE values are higher than the experimental standard deviation, the model still exhibits good local

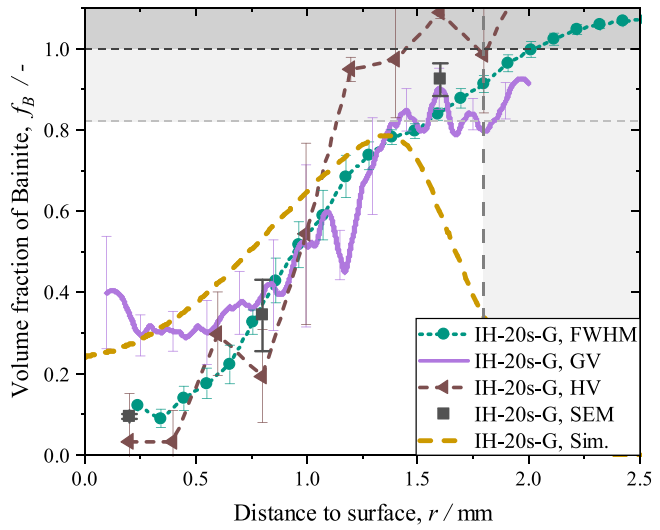

Fig. 18. Outcome of the present simulation model (Sim.) in comparison with earlier experimental data [27]. The values of f_B were obtained from the full width at half maximum (FWHM) of the intensity profile of the X-ray diffraction pattern, from a gray value analysis of the micrograph (GV), from an evaluation based on the measured hardness (HV), and from the assessment of an image acquired with a scanning electron microscope (SEM).

consistency with the measurements, as the predicted hardness profiles lie predominantly within the range of the experimental data. The greatest deviation between the model and the experiments is observed for the IH-RT-H sample. This is primarily because the present simulation model was not developed to describe martensite transformation at the relatively low cooling rates that occur in a fully austenitised component subjected to direct quenching. As a result, the actual extent of the self-tempering effect may be underestimated by the hardness model used. In contrast, the predictions for bainite transformation show substantially lower deviation, which can be attributed to the austempering step, since the reduced temperature differences during quenching to room temperature also reduce self-tempering. Potential extensions and improvements in martensite transformation within the model will be addressed in future work.

Furthermore, comparing the experimental and simulated results raises the question of how to incorporate standard deviation into the model. Taking into account variations in d_γ and in chemical composition would induce a spread of approximately ±100 HV. Similarly, hardness measurements of mixed microstructures are strongly influenced by local heterogeneities. More importantly, the model accurately reflects the fundamental trends and the dependence of hardness on the process parameters. This makes it particularly suitable for process optimisation, as relative variations and sensitivities can be predicted with confidence. As a result, the key advantage of the model is not in accurately predicting absolute magnitudes but in its consistent characterisation of the fundamental physical relationships and their associated trends.

In summary, the simulated and experimentally measured hardness profiles in Fig. 15 demonstrate that f_B can be modelled by defining d_γ and t_{iso}. As a limitation of the model, it must be noted that the formulation of d_γ is explicitly derived for AISI 4140 and high heating rates. Therefore, its use for materials with different chemical compositions is limited and can only be presumed to a certain extent. The same restriction holds for the additional fit parameters λ and $w_{C,B}$. Nevertheless, it has been shown that the bainite transformation model can be applied to spatially graded microstructures and offers new and promising possibilities for optimising the inductive short-time austempering process.

5. Conclusion

The results of this study showed the possibility of applying the bainite transformation model of Van Bohemen [24] to homogeneously distributed and spatially graded martensitic–bainitic microstructures of AISI 4140. The model successfully replicated the experimental bainite transformation at laboratory scale, achieving an average RMSE of less than 3 % in predicting the evolution of f_B for isothermal transformation temperatures up to 500 °C. When applied on the component scale, the model successfully reproduced the trends of the hardness depth profiles for two different heating strategies and four different quenching strategies, achieving an overall RMSE of 42 HV1 for homogeneously heat-treated samples and 41 HV1 for the surface-hardened samples. Despite the deviation observed, the model demonstrates considerable potential for improving process optimisation. Three main aspects can be defined for the model:

- The transformation kinetics model developed for homogeneously distributed martensitic–bainitic microstructures can be extended and applied to spatially graded microstructures at the component scale.
- It was shown that within spatially graded microstructures, bainitic transformation kinetics is highly sensitive to the parent austenite grain size distribution. The model presented for d_γ is in good agreement with the experimental results for AISI 4140.
- A detailed analysis of the model leads to the assumption that the autocatalytic factor λ is not directly dependent on the parent austenite grain size d_γ. The effect of d_γ on the transformation rate is included in the nucleation factor κ.

The experimental results and the model support the hypothesis that the bainite transformation is strongly controlled by the morphology of its subunits. However, the model is expected to lose reliability when the morphology deviates from a lath-like geometry at temperatures exceeding 500 °C. Overall, this investigation provides a crucial basis for the application of inductive austempering to optimise manufacturing operations, tailor component hardness profiles, and thereby potentially extend component service life.

Funding

Funded by the Deutsche Forschungsgemeinschaft (DFG, German Research Foundation) – SFB 1574-471687386.

Declaration of Generative AI and AI-assisted technologies in the writing process

During the preparation of this manuscript, the authors used DeepL (DeepL SE, Germany) and Writefull (Writefull, UK) to enhance its language and readability. All outputs were subsequently reviewed and revised where necessary, and the authors assume full responsibility for the final content.

Declaration of competing interest

The authors declare that they have no known competing financial interests or personal relationships that could have appeared to influence the work reported in this paper.

Acknowledgments

The authors would like to thank the Institute for Applied Materials (IAM-ZM) at the Karlsruhe Institute of Technology (KIT) for the use of the SEM-EBSD. The authors acknowledge the chemical analysis by ICP-OES conducted at the Institute for Applied Materials (IAM-AWP), Karlsruhe Institute of Technology (KIT).

Appendix. Attachment

See Tables 5 and 6.

Table 5
Overview of the parameters required to express κ. When working with the chemical composition, these parameters were denoted by w_i, representing the mass percentage of alloying element i.

Parameter	Description or calculation	Unit	Source
V_m	molar volume of iron: 7.1×10^{-6}	m^3mol^{-1}	[72]
ν^*	attempt frequency; assumed constant: 1×10^{13}	s^{-1}	[72]
$6N_sV_n$	overall constant in expression for df/dt; = 12×10^{-9}	m	[24]
R	Ideal gas constant: 8.314	$Jmol^{-1}K^{-1}$	
$\Delta G^{\alpha\rightarrow\gamma}$	driving force for diffusionless $\alpha \rightarrow \gamma$ transformation	$Jmol^{-1}$	[24]
Γ_M	$d(\Delta G^{\alpha\rightarrow\gamma})/dT$ within the martensite temperature range: 7.22	$Jmol^{-1}K^{-1}$	[24]
Γ_B	$d(\Delta G^{\alpha\rightarrow\gamma})/dT$ within the bainite temperature range: 6.23	$Jmol^{-1}K^{-1}$	[24]
Q_b	effective activation energy: $= 89w_C + 10w_{Mn} + 12w_{Si} + 2w_{Cr} + 1w_{Ni} + 29w_{Mo}$	$kJmol^{-1}$	[41]
$K_1\Gamma$	weighted Γ: $= (170kJmol^{-1} - Qb)/(705\ K)$	$kJmol^{-1}\ K^{-1}$	[41]
M_S	martensite start-temperature: $= 565 - (31w_{Mn} + 13w_{Si} + 10w_{Cr} + 18w_{Ni} + 12w_{Mo}) -600(1 - \exp(-0.96w_C))$	°C	[30]
B_S	bainite start-temperature: $= 839 - (86w_{Mn} + 23w_{Si} + 67w_{Cr} + 33w_{Ni} + 75w_{Mo}) -270(1 - \exp(-1.33w_C))$	°C	[30]
B_{S^*}	bainite start-temperature of stabilised austenite: $= B_S - (\Delta B_{S,\sigma_\gamma} + \Delta B_{S,B})$	°C	[24]
$\Delta B_{S,\sigma_\gamma}$	decrease in B_S related to the dependency of σ_y to T: $= (\sigma_{\gamma,T} - \sigma_{\gamma,B_S})/\Gamma_B V_m$	K	[24]
$\sigma_{\gamma,25\,°C}$	austenite yield strength at 25 °C: $= 87.8 + 254w_C + 15.1w_{Si} + 2.5w_{Cr} + 14.5w_{Mo} + 18.5w_V +4.5w_W + 40w_{Nb} + 5.4w_{Al} + 26.2w_{Ti} + 10.5/\sqrt{d^\gamma}$	MPa	[42]
$\sigma_{\gamma,T}$	austenite yield strength at temperature T: $= \sigma_{\gamma,25\,°C}[1 - 2.2(T-25)/10^3 + 4.2(T-25)^2/10^6 -3(T-25)^3/10^9]$	MPa	[42]
σ_{lim}	limit of austenite yield strength: $= 66.6 + 140w_C - 1.1w_{Mn} + 1.8w_{Si} + 2.6w_{Cr} + 7.7w_{Mo} -0.8w_{Ni} + 1.5_{Al} + 2.2w_{Co} + 4.9/\sqrt{d_\gamma}$	MPa	[42]
$\Delta B_{S,B}$	decrease in B_S due to the stabilisation of austenite by prior bainite: $= 0.7\Delta G_{e,Ms}/\Gamma_B$	K	[24]
$\Delta G_{e,Ms}$	increase in the elastic strain energy G_e of martensite due to stabilisation of austenite by prior bainite: $= \Gamma_M ln(1 - f_B)/\beta_{Ms,B}$	$Jmol^{-1}$	[24]
$\beta_{Ms,B}$	parameter controlling decrease in bainite fraction dependend start-temperature T^*_{KM} in Koistinen–Marburger equation with fraction bainite: $= \alpha_M[p_C(T - M_S) + 1]$	K^{-1}	[24]
α_M	rate parameter in Koistinen–Marburger equation: $= 27.2 - (0.14w_{Mn} + 0.21w_{Si} + 0.11w_{Cr} + 0.08w_{Ni} +0,05w_{Mo}) - 19.8[1 - \exp(-1.56w_C)]$	K^{-1}	[30]
p_C	rate parameter in Koistinen–Marburger equation: $= 0.051 - 0.044[1 - \exp(-3w_C)]$	K^{-1}	[24]
$G_{e,0}$	elastic strain energy of the first formed bainite at $T < Bs$: $= (\sigma_{\gamma,T} - \sigma_{\gamma,B_S})V_m + 400Jmol^{-1}$	$Jmol^{-1}$	[24]
$\Delta G_{e,B}$	increase in G_e of bainite due to stabilisation of austenite by prior bainite: $= 0.7\Delta G_{e,Ms}$	$Jmol^{-1}$	[24]

Table 6
Results for the average parent austenite grain size of a preliminary dilatometer study to model the austenite grain growth in AISI 4140 after Wang et al. [16] with different holding temperatures and elevated heating rates. The grains sizes were determined using thermal etching and the line cutting method.

t_{hold}	950 °C, 250 Ks^{-1}	1000 °C, 250 Ks^{-1}	1050 °C, 250 Ks^{-1}	1050 °C, 500 Ks^{-1}
2 s	(6.3 ± 5.0) µm	(9.1 ± 7.0) µm	(12.6 ± 8.0) µm	(10.4 ± 6.0) µm
4 s	(8.5 ± 6.0) µm	(9.7 ± 7.0) µm	(13.8 ± 8.0) µm	(12.0 ± 7.0) µm
6 s	(10.0 ± 6.0) µm	(10.2 ± 7.0) µm	(14.4 ± 8.0) µm	(12.1 ± 8.0) µm

References

[1] Zoch H-W. Randschichtverfestigung - Verfahren und Bauteileigenschaften. HTM J Heat Treat Mater 1995;50(5):287–94h. http://dx.doi.org/10.1515/htm-1995-500507.

[2] Mühl F, Jarms J, Kaiser D, Dietrich S, Schulze V. Tailored bainitic-martensitic microstructures by means of inductive surface hardening for AISI4140. Mater Des 2020;195:108964. http://dx.doi.org/10.1016/j.matdes.2020.108964.

[3] Chen J-Z, Zhang B. Effect of bainite volume fraction on fatigue properties of bainite/martensite dual phase EA4t steel. J Miner Met Mater Eng 2019;5:12–21.

[4] Liu R, Zhang ZJ, Li LL, An XH, Zhang ZF. Microscopic mechanisms contributing to the synchronous improvement of strength and plasticity (SISP) for TWIP copper alloys. Sci Rep 2015;5(1):9550. http://dx.doi.org/10.1038/srep09550.

[5] Wang Y, Sun J, Jiang T, Sun Y, Guo S, Liu Y. A low-alloy high-carbon martensite steel with 2.6 GPa tensile strength and good ductility. Acta Mater 2018;158:247–56. http://dx.doi.org/10.1016/j.actamat.2018.07.060.

[6] Schüßler P, Dollhofer B, Krämer C, Englert L, Hinrichs F, Schulze V, Dietrich S. Influence of base plate preheating temperature on fatigue strength of AISI 4140 manufactured by laser powder bed fusion. J Mater Res Technol 2025;35:1358–68. http://dx.doi.org/10.1016/j.jmrt.2025.01.073.

[7] Chai G. The formation of subsurface non-defect fatigue crack origins. Int J Fatigue 2006;28(11):1533–9. http://dx.doi.org/10.1016/j.ijfatigue.2005.06.060.

[8] Yu Y, Gu J, Bai B, Liu Y, Li S. Very high cycle fatigue mechanism of carbide-free bainite/martensite steel micro-alloyed with nb. Mater Sci Eng: A 2009;527(1–2):212–7. http://dx.doi.org/10.1016/j.msea.2009.08.024.

[9] Zhao Z, Tong T, Liang J, Yin H, Zhao A, Tang D. Microstructure, mechanical properties and fracture behavior of ultra-high strength dual-phase steel. Mater Sci Eng: A 2014;618:182–8. http://dx.doi.org/10.1016/j.msea.2014.09.005.

[10] Bhadeshia H. The nature, mechanism and properties of strong bainite, procceding of the 1st international symposium on steel science (IS3 2007). Iron Steel Inst Jpn 2007.

[11] Liedl U, Traint S, Werner E. An unexpected feature of the stress–strain diagram of dual-phase steel. Comput Mater Sci 2002;25(1–2):122–8. http://dx.doi.org/10.1016/S0927-0256(02)00256-2.

[12] Fereiduni E, Ghasemi Banadkouki S. Reliability/unreliability of mixture rule in a low alloy ferrite–martensite dual phase steel. J Alloys Compd 2013;577:351–9. http://dx.doi.org/10.1016/j.jallcom.2013.05.209.

[13] Paul SK. Effect of martensite volume fraction on stress triaxiality and deformation behavior of dual phase steel. Mater Des 2013;50:782–9. http://dx.doi.org/10.1016/j.matdes.2013.03.096.

[14] Tomita Y, Okabayashi K. Improvement in lower temperature mechanical properties of 0.40 pct C-Ni-Cr-Mo ultrahigh strength steel with the second phase lower bainite. Met Trans A 1983;14(2):485–92.

[15] Sellars CM, Whiteman JA. Recrystallization and grain growth in hot rolling. Met Sci 1979;13(3–4):187–94. http://dx.doi.org/10.1179/msc.1979.13.3-4.187.

[16] Wang L, Qian D, Guo J, Pan Y. Austenite grain growth behavior of AISI 4140 alloy steel. Adv Mech Eng 2013;5:762890. http://dx.doi.org/10.1155/2013/762890.

[17] Javaheri V, Kolli S, Grande B, Porter D. Insight into the induction hardening behavior of a new 0.40% C microalloyed steel: Effects of initial microstructure and thermal cycles. Mater Charact 2019;149:165–83. http://dx.doi.org/10.1016/j.matchar.2019.01.029.

[18] Barford J, Owen W. The effect of austenite grain size and temperature on the rate of bainite transformation. J Iron Steel Inst 1961;197(2):359–60.

[19] Yang J. Thermodynamics of the acicular ferrite transformation in alloy-steel weld deposits. Adv Weld Scinence Technol 1987;187–91.

[20] Bhadeshia HKDH, Christian JW. Bainite in steels. Met Trans A 1990;21(3):767–97. http://dx.doi.org/10.1007/BF02656561.

[21] Matsuzaki A, Bhadeshia H. Effect of austenite grain size and bainite morphology on overall kinetics of bainite transformation in steels. Mater Sci Technol 1999;15(5):518–22. http://dx.doi.org/10.1179/026708399101506210.

[22] Avila DDS, Offerman SE, Santofimia MJ. Modeling the effect of prior austenite grain size on bainite formation kinetics. Acta Mater 2024;266:119656. http://dx.doi.org/10.1016/j.actamat.2024.119656.

[23] Winderlich B. Das Konzept der lokalen Dauerfestigkeit und seine Anwendung auf martensitische Randschichten, insbesondere Laserhärtungsschichten. Mater Werkst 1990;21(10):378–89. http://dx.doi.org/10.1002/mawe.19900211006.

[24] Van Bohemen S. Bainite growth retardation due to mechanical stabilisation of austenite. Materialia 2019;7:100384. http://dx.doi.org/10.1016/j.mtla.2019.100384.

[25] Ulrich C, Günther S, Becker N, Schubert V, Vetter B, Leyens C, Schlecht B. High strength tempered 42CrMo4 for shafts in drive technology. Forsch Ingenieurwes 2025;89(1):59. http://dx.doi.org/10.1007/s10010-025-00818-x.

[26] Schulze V. Modern mechanical surface treatment: states, stability, effects. Weinheim: Wiley-VCH; 2006.

[27] Dollhofer B, Krämer C, Nouri N, Dietrich S, Schulze V. Characterization of martensitic-bainitic mixed microstructures created by inductive short time austempering of AISI 4140. In: Proceedings of the 29th international federation for heat treatment and surface engineering world congress. Cleveland, Ohio, USA; 2024, p. 41–9. http://dx.doi.org/10.31399/asm.cp.ifhtse2024p0041.

[28] Rose A, Hougardy HP. Atlas zur Wärmebehandlung der Stähle. 2 / von Adolf Rose und Hans Hougardy. Düsseldorf: Stahleisen; 1972.

[29] Van Bohemen SMC, Hanlon DN. A physically based approach to model the incomplete bainitic transformation in high-Si steels. Int J Mater Res 2012;103(8):987–91. http://dx.doi.org/10.3139/146.110744.

[30] Van Bohemen SMC. Bainite and martensite start temperature calculated with exponential carbon dependence. Mater Sci Technol 2012;28(4):487–95. http://dx.doi.org/10.1179/1743284711Y.0000000097.

[31] E04 Committee. Practice for X-ray determination of retained austenite in steel with near random crystallographic orientation. 2023, http://dx.doi.org/10.1520/e0975-22.

[32] Hielscher R, Schaeben H. A novel pole figure inversion method: specification of the *MTEX* algorithm. J Appl Crystallogr 2008;41(6):1024–37. http://dx.doi.org/10.1107/S0021889808030112.

[33] Niessen F, Nyyssönen T, Gazder AA, Hielscher R. Parent grain reconstruction from partially or fully transformed microstructures in \emphMTEX. J Appl Crystallogr 2022;55(1):180–94. http://dx.doi.org/10.1107/S1600576721011560.

[34] DINDeutsches Institut für Normung ev. DIN EN ISO 6507-1:2024-01, Metallische Werkstoffe_-Härteprüfung nach Vickers_- Teil_1: Prüfverfahren (ISO_6507-1:2023); Deutsche Fassung EN_ISO_6507-1:2023. 2024, http://dx.doi.org/10.31030/3503781.

[35] Davenport ES, Bain EC. Transformation of austenite at constant subcritical temperatures. Met Trans 1970;1(12):3503–30. http://dx.doi.org/10.1007/BF03037892.

[36] Hillert M. The nature of bainite. ISIJ Int 1995;35(9):1134–40. http://dx.doi.org/10.2355/isijinternational.35.1134.

[37] Bhadeshia H, Edmonds D. The mechanism of bainite formation in steels. Acta Metall 1980;28(9):1265–73. http://dx.doi.org/10.1016/0001-6160(80)90082-6.

[38] Fielding LCD. The bainite controversy. Mater Sci Technol 2013;29(4):383–99. http://dx.doi.org/10.1179/1743284712Y.0000000157.

[39] Song W, Prahl U, Bleck W, Mukherjee K. Phase-field simulations of bainitic phase transformation in 100cr6. Suppl Proc 2011;417–25.

[40] van Bohemen SMC, Sietsma J. Modeling of isothermal bainite formation based on the nucleation kinetics. Int J Mater Res 2008;99(7):739–47. http://dx.doi.org/10.3139/146.101695.

[41] Van Bohemen S. Modeling start curves of bainite formation. Metall Mater Trans A 2010;41(2):285–96. http://dx.doi.org/10.1007/s11661-009-0106-9.

[42] Van Bohemen S. Exploring the correlation between the austenite yield strength and the bainite lath thickness. Mater Sci Eng: A 2018;731:119–23. http://dx.doi.org/10.1016/j.msea.2018.06.041.

[43] Ravi AM, Sietsma J, Santofimia MJ. Exploring bainite formation kinetics distinguishing grain-boundary and autocatalytic nucleation in high and low-si steels. Acta Mater 2016;105:155–64. http://dx.doi.org/10.1016/j.actamat.2015.11.044.

[44] Schwenk M. Entwicklung und validierung eines numerischen simulationsmodells zur beschreibung der induktiven ein- und zweifrequenzrandschichthärtung am beispiel von vergütetem 42crmo4. 2012, http://dx.doi.org/10.5445/IR/1000029378.

[45] Kaiser D. Experimentelle untersuchung und simulation des kurzzeitanlassens unter berücksichtigung thermisch randschichtgehärteter zustände am beispiel von 42CrMo4 (Ph.D. thesis), Karlsruhe; 2019, http://dx.doi.org/10.5445/IR/1000100278.

[46] Kaiser D, Damon J, Mühl F, de Graaff B, Kiefer D, Dietrich S, Schulze V. Experimental investigation and finite-element modeling of the short-time induction quench-and-temper process of AISI 4140. J Mater Process Technol 2020;279:116485. http://dx.doi.org/10.1016/j.jmatprotec.2019.116485.

[47] Mühl F, Damon J, Dietrich S, Schulze V. Simulation of induction hardening: Simulative sensitivity analysis with respect to material parameters and the surface layer state. Comput Mater Sci 2020;184:109916. http://dx.doi.org/10.1016/j.commatsci.2020.109916.

[48] Schüßler P, Damon J, Mühl F, Dietrich S, Schulze V. Laser surface hardening: A simulative study of tempering mechanisms on hardness and residual stress. Comput Mater Sci 2023;221:112079. http://dx.doi.org/10.1016/j.commatsci.2023.112079.
[49] Dollhofer B, Dietrich S, Schulze V. Improvement of an electromagnetic-thermal-mechanical coupled simulation for the optimization of complex processes in induction hardening, 64, netsu-shori. J. Jpn. Soc. Heat Treat. 2024;66–71.
[50] Mioković T, Schwarzer J, Schulze V, Vöhringer O, Löhe D. Description of short time phase transformations during the heating of steels based on high-rate experimental data. J Phys IV (Proceedings) 2004;120:591–8. http://dx.doi.org/10.1051/jp4:2004120068.
[51] Mioković T, Schulze V, Vöhringer O, Löhe D. Prediction of phase transformations during laser surface hardening of AISI 4140 including the effects of inhomogeneous austenite formation. Mater Sci Eng: A 2006;435–436:547–55. http://dx.doi.org/10.1016/j.msea.2006.07.037.
[52] Hollomon JH, Jaffe LD. Time-temperature relations in tempering steel. Trans AIME 1945;162:223–49.
[53] Gomes C, Kaiser A-L, Bas J-P, Aissaoui A, Piette M. Predicting the mechanical properties of a quenched and tempered steel thanks to a "tempering parameter". Rev Metall 2010;107(7–8):293–302. http://dx.doi.org/10.1051/metal/2010061.
[54] Kaiser D, De Graaff B, Dietrich S, Schulze V. Investigation of the precipitation kinetics and microstructure evolution of martensitic AISI 4140 steel during tempering with high heating rates. Met Res Technol 2018;115(4):404. http://dx.doi.org/10.1051/metal/2018026.
[55] Matsuda H, Bhadeshia HKDH. Kinetics of the bainite transformation. Proc R. Soc Lond A 2004;460(2046):1707–22. http://dx.doi.org/10.1098/rspa.2003.1225.
[56] Chatterjee S, Wang H-S, Yang JR, Bhadeshia HKDH. Mechanical stabilisation of austenite. Mater Sci Technol 2006;22(6):641–4. http://dx.doi.org/10.1179/174328406X86128.
[57] Seo S-W, Jung G-S, Lee JS, Bae CM, Bhadeshia HKDH, Suh D-W. Ausforming of medium carbon steel. Mater Sci Technol 2015;31(4):436–42. http://dx.doi.org/10.1179/1743284714Y.0000000574.
[58] Fisher JC, Hollomon JH, Turnbull D. Kinetics of the austenite → martensite transformation. J Oper Manage 1949;1(10):691–700. http://dx.doi.org/10.1007/BF03398922.
[59] Jimenez-Melero E, Van Dijk N, Zhao L, Sietsma J, Offerman S, Wright J, Van Der Zwaag S. Characterization of individual retained austenite grains and their stability in low-alloyed TRIP steels. Acta Mater 2007;55(20):6713–23. http://dx.doi.org/10.1016/j.actamat.2007.08.040.
[60] Hidalgo J, Findley K, Santofimia M. Thermal and mechanical stability of retained austenite surrounded by martensite with different degrees of tempering. Mater Sci Eng: A 2017;690:337–47. http://dx.doi.org/10.1016/j.msea.2017.03.017.
[61] Nakada N, Ishibashi Y, Tsuchiyama T, Takaki S. Self-stabilization of untransformed austenite by hydrostatic pressure via martensitic transformation. Acta Mater 2016;110:95–102. http://dx.doi.org/10.1016/j.actamat.2016.03.048.
[62] Garboczi EJ, Snyder KA, Douglas JF, Thorpe MF. Geometrical percolation threshold of overlapping ellipsoids. Phys Rev E 1995;52(1):819–28. http://dx.doi.org/10.1103/PhysRevE.52.819.
[63] Timokhina IB, Liss KD, Raabe D, Rakha K, Beladi H, Xiong XY, Hodgson PD. Growth of bainitic ferrite and carbon partitioning during the early stages of bainite transformation in a 2 mass% silicon steel studied by *in situ* neutron diffraction, TEM and APT. J Appl Crystallogr 2016;49(2):399–414. http://dx.doi.org/10.1107/S1600576716000418.
[64] Bhadeshia HKDH, Edmonds DV. The bainite transformation in a silicon steel. Metall Trans A 1979;10(7):895–907. http://dx.doi.org/10.1007/BF02658309.
[65] Chang L, Bhadeshia HKDH. Metallographic observations of bainite transformation mechanism. Mater Sci Technol 1995;11(2):105–8. http://dx.doi.org/10.1179/mst.1995.11.2.105.
[66] Van Bohemen S. Autocatalytic nature of the bainitic transformation in steels: a new hypothesis. Phil Mag 2013;93(4):388–408. http://dx.doi.org/10.1080/14786435.2012.721570.
[67] Goodenow R, Barkalow R, Hehemann R. Bainite transformations in hypoeutectoid steels. Phys Prop Martensite Bainite Spec Rep 1969;93:135–41.
[68] Christian J. The theory of transformations in metals and alloys. Mater Today 2003;6(3):53. http://dx.doi.org/10.1016/S1369-7021(03)00335-3.
[69] Caballero F, Miller M, Babu S, Garciamateo C. Atomic scale observations of bainite transformation in a high carbon high silicon steel. Acta Mater 2007;55(1):381–90. http://dx.doi.org/10.1016/j.actamat.2006.08.033.
[70] Gouné M, Bouaziz O, Allain S, Zhu K, Takahashi M. Kinetics of bainite transformation in heterogeneous microstructures. Mater Lett 2012;67(1):187–9. http://dx.doi.org/10.1016/j.matlet.2011.09.053.
[71] Ueji R, Kimura Y, Ushioda K, Ohmura T, Inoue T. Bainite transformation and resultant tensile properties of 0.6%c low alloyed steels with different prior austenite grain sizes. ISIJ Int 2021;61(2):582–90. http://dx.doi.org/10.2355/isijinternational.ISIJINT-2020-389.
[72] Pati S, Cohen M. Nucleation of the isothermal martensitic transformation. Acta Metall 1969;17(3):189–99. http://dx.doi.org/10.1016/0001-6160(69)90058-3.